ASCE Author Proofs

Important Notice to Authors

Attached is a PDF proof of your forthcoming article in **International Journal of Geomechanics**. The manuscript ID number is **GMENG-6404**.

No further publication processing will occur until we receive your response to this proof. Please return any corrections within 48 hours of receiving the download email. Your paper will be published in its final form upon receipt of these corrections. You will have no further opportunities to review your proof or to request changes after this stage.

Information and Instructions

- The graphics in your proof have been down-sampled to produce a more manageable file size and generally represent the online presentation. Higher resolution versions will appear in print.
- Proofread your article carefully, as responsibility for detecting errors lies with the author.
- Mark or cite all corrections on your proof copy only.
- Corrections should be completed within 48 hours after receipt of this message.
- If no errors are detected, **you are still required to log in, make note in the proof, and finalize the article to indicate that it is okay** to be published as is.
- You will receive a message confirming receipt of your corrections within 48 hours.

Questions and Comments to Address

The red numbers in the margins correspond to queries listed on the last page of your proof. Please address each of these queries when responding with your proof corrections.

Return your Proof Corrections

- Web: If you accessed this proof online, follow the instructions on the Web page to submit corrections.
- E-mail: Send corrections to ascejournals@novatechset.com. Include the manuscript ID GMENG-6404 in the subject line. Please do not provide a revised manuscript.

Please annotate and complete your proof review within 48 hours. Should this not be possible or should you encounter any problems or have further questions, please contact the Journal Production Manager at ascejournals@novatechset.com and include GMENG-6404 in the subject line.

ASCE Open Access

Authors may choose to publish their papers through ASCE Open Access, making the paper freely available to all readers via the ASCE Library website. ASCE Open Access papers will be published under the Creative Commons-Attribution Only (CC-BY) License. The fee for this service is USD 2,000 and must be paid prior to publication. If you indicate Yes, you will receive a follow-up message with payment instructions. If you indicate No, your paper will be published in the typical subscribed-access section of the Journal.

Selecting Yes does not commit you to publishing your article as Open Access. You will have the option to cancel the Open Access process later. If you are unsure, we recommend selecting Yes. If you select No now, your paper will be published online shortly after your proof corrections are received. After a journal article is published, its copyright status cannot change until two years have passed. For further information, please see https://ascelibrary.org/page/openaccessoptionsandrights.

Color Figures

Figures containing color will appear in color in the online journal. All figures will be grayscale in the printed journal unless you have agreed to pay the color figure surcharge and the relevant figure caption indicates "(Color)". For figures that will be in color online but grayscale in print, please ensure that the text and captions do not describe the figures using colors.

If you have indicated that you will be printing color figures in color, you will receive a notification with a link to the payment system. Until payment is received or color printing is canceled, your article will not be published.

Reprints

If you would like to order reprints of your article, please visit https://www.asce.org/reprints.

Experimental and Numerical Investigation on the Dynamic Failure Envelope and Cracking Mechanism of Precompressed Rock under Compression-Shear Loads

Yuan Xu[1]; Antonio Pellegrino[2]; Feng Dai[3]; and Hongbo Du[4]

Abstract: The complex response of underground geomaterials subjected to dynamic disturbance arises from the microstructure redistribution under high in- situ stress and the resulting fracture behaviors at multiaxial stress states. Inclined specimens were employed in an axially constrained split Hopkinson pressure bar (SHPB) system to achieve a combination of compression-shear stress states and static-dynamic loads. The loading rate under investigation ranged from 500 to 4,000 GPa/s, along with the axial prestress of 7, 21, 35, 49, and 63 MPa on specimens with an inclination of 0°, 3°, 5°, and 7°. The modified SHPB experimentation and discrete-element method modeling were implemented to unravel the combined effects of the loading rate, preload, and stress path on the failure mechanism of sandstone specimens involving the failure strength and envelope, fracturing pattern, fragmentation, and microcracking process. The positive rate dependence of the failure strength and Drucker–Prager envelope was observed. The preload showed double effects on the failure strength, indicated by an upper bound of the failure envelope as it expanded with the increasing preload. The microdamage accumulated during preloading and the global stress field collectively influenced the failure pattern of the inclined specimen, altering from a shear fracturing mode under dynamic loading or high-preload static-dynamic loading to an axial splitting mode near the specimen surface under low-preload static-dynamic loading.
DOI: 10.1061/(ASCE)GM.1943-5622.0002196.

Author keywords: Static-dynamic; Compression-shear; SHPB; Failure envelope; Microcracking.

Introduction

With the development of deep underground engineering involving resource exploitation, transportation, and safety defense, an increasing number of phenomena (e.g., rockbursts) that are barely observed in shallow rock engineering have been largely reported (Ranjith et al. 2017; Khosravi and Simon 2018; Jiang et al. 2021). Resulting from the locked-in stress of tectonic activities and the weight of the overlying strata, rock at depth is under varying in situ stress that scales with the depth of the site (Hoek and Brown 1980; Chattaraj et al. 2013). Additional engineering or natural dynamic disturbances, such as drilling and blasting, ballistic impact, faulting, and earthquake, can be coupled with the initial geostress, resulting in rock mass subjected to combined static-dynamic loads (Weng et al. 2018). Owing to geological discontinuities that locally transform the stress state (Paliwal and Ramesh 2008), rock mass is commonly at compression-shear stress states rather than true uniaxial conditions. The complex response of deep underground rock subjected to dynamic disturbance arises from the high in situ stress and multiaxial stress states. Knowledge of the dynamic behaviors and failure mechanism of precompressed rock at compression-shear stress states is of fundamental significance to understanding constitutive models and practical importance to optimizing engineering designs.

Simulations of the combined static-dynamic loads imposed on rock at multiaxial stress states in a laboratory environment can be traced back to the research by Christensen et al. (1972) and Lindholm et al. (1974). The split Hopkinson pressure bar (SHPB), which has been extensively developed up to date for material characterization at a high strain rate range of 10^1–10^4 s^{-1} (Field et al. 2004; Gama et al. 2004; Zhang and Zhao 2014), was modified with a hydrostatic confining chamber to simulate one type of rockburst caused by the superposition of the exterior dynamic disturbance with the interior stress of rock. Following this, a variety of experimental approaches based on SHPB techniques have been developed to address the multiaxial static-dynamic loading events, but they mainly focus on the confining techniques by means of hydraulic pressure chamber (Li et al. 2008; Frew et al. 2010; Hokka et al. 2016; Gong et al. 2019; Du et al. 2020), metallic ring (Chen and Ravichandran 1997; Forquin et al. 2008), or screw-driven platens (Paliwal et al. 2008; Farbaniec et al. 2017). Such studies simplified the dynamic load to coincide with one principal stress of the static confinement and hence failed to reflect the realistic complexity of the stress state of rock mass at depth. Recently, Cadoni et al. (2015) and Liu et al. (2020) extend the SHPB techniques to build a true triaxial dynamic testing system, where a cubic specimen, which has been installed in an axially confined SHPB system, is additionally constrained on the remaining faces by another four transmitted bars. The triaxial dynamic load is thus composed of the axial stress wave launched by SHPB and the spontaneous lateral stress waves resulting from the

[1]Former Ph.D. Candidate, State Key Laboratory of Hydraulics and Mountain River Engineering, College of Water Resources and Hydropower, Sichuan Univ., Chengdu, Sichuan 610065, China; Postdoctoral Research Associate, Dept. of Engineering Science, Univ. of Oxford, Oxford OX1 3PJ, UK. Email: yuan.xu@eng.ox.ac.uk

[2]Lecturer, Dept. of Engineering Science, Univ. of Oxford, Oxford OX1 3PJ, UK. Email: antonio.pellegrino@eng.ox.ac.uk

[3]Professor, State Key Laboratory of Hydraulics and Mountain River Engineering, College of Water Resources and Hydropower, Sichuan Univ., Chengdu, Sichuan 610065, China (corresponding author). Email: fengdai@scu.edu.cn

[4]Lecturer, National Engineering Research Center for Inland Waterway Regulation, Chongqing Jiaotong Univ., Chongqing 400074, China. Email: duhongbo@cqjtu.edu.cn

Note. This manuscript was submitted on November 1, 2020; approved on July 15, 2021No Epub Date. Discussion period open until 0, 0; separate discussions must be submitted for individual papers. This paper is part of the ***International Journal of Geomechanics***, © ASCE, ISSN 1532-3641.

lateral expansion and confining. Inclination is another approach to achieve compression-induced multiaxial loading. By inclining the specimen-loading interface with respect to the loading direction, a shear component can be introduced and thus complicate the stress path. This technique has been implemented in SHPB by means of inclined specimens (Nie et al. 2007; Xu and Dai 2018) or bevel bar ends (Zhou et al. 2018) and in a gas gun via oblique targets (Abou-Sayed et al. 1976; Gupta 1983) for high-rate testing, but very few studies (Xu et al. 2020) have been undertaken in the regime of combined static-dynamic loading.

Most computational models of rock for engineering purposes idealize the rock material as a continuum and represent microstructural damage by averaged material degradation in the macroscopic constitutive relationships. In contrast to these phenomenological approaches to describing the mechanical behaviors of rock, the discrete-element method (DEM) provides a direct way to understand the behaviors by focusing on the grain-scale microstructure of the rock material and representing damage via the formation and interaction of microcracks (Jing 2003; Potyondy and Cundall 2004). The micromechanical basis of DEM allows the synthetic material to possess much disorder in the microstructural complexity, including the size and shape of the grains, the deformability and strength of the grains and cements, the degree of packing and cementation, and heterogeneous force chain transmission. All of these microscopic features, many of which evolve under loading, collectively influence and regulate the macroscopic behaviors of rock and thereby allow the hypotheses of the effects of the microstructure to be examined. DEM has been successfully developed to reproduce the fracture and failure behaviors of rock in terms of, for example, crack nucleation (Hazzard et al. 2000), acoustic emission (Hazzard and Young 2000), cohesive damage-plasticity (Nguyen et al. 2017), grain interlocking (Scholtès and Donzé 2013), and multiscale fracturing (Li et al. 2018).

Experimental and numerical simulations of sandstone subjected to combined static-dynamic loads at multiaxial stress states are conducted in this study. The far-field one-dimensionally combined static-dynamic load is implemented by an axially confined SHPB system. The inclined specimen method is utilized in the modified SHPB to introduce different combinations of compression-shear loads and thus to unravel the combined effects of the loading rate, preload, and stress path on the multiaxial failure mechanism of sandstone specimens. It is a further study of the previous research where the validity of a particular 7° inclined specimen in axially constrained SHPB testing was critically addressed involving dynamic equilibrium, stress uniform, and interfacial friction effects (Xu et al. 2020). This study examines three more inclinations so as to generalize the data reduction method for inclined specimens to accommodate a wide range of inclinations and to assess the stress path dependence of the failure strength and fracturing process under combined static-dynamic loading. The Drucker–Prager failure envelope is therefore constructed to reveal the influence of the loading rate and preload. The DEM-based micromechanical modeling demonstrates its ability to reproduce the failure pattern and the fragmentation of compression-shear specimens under combined static-dynamic loading. The interior microcracking process of the specimen under complex loading conditions is captured and contributes to revealing the intrinsic microdamage mechanism.

Experimental Methodology

Specimen Preparation

The rock material under investigation was sandstone drilled out of the same rock block quarried at an active earthquake region

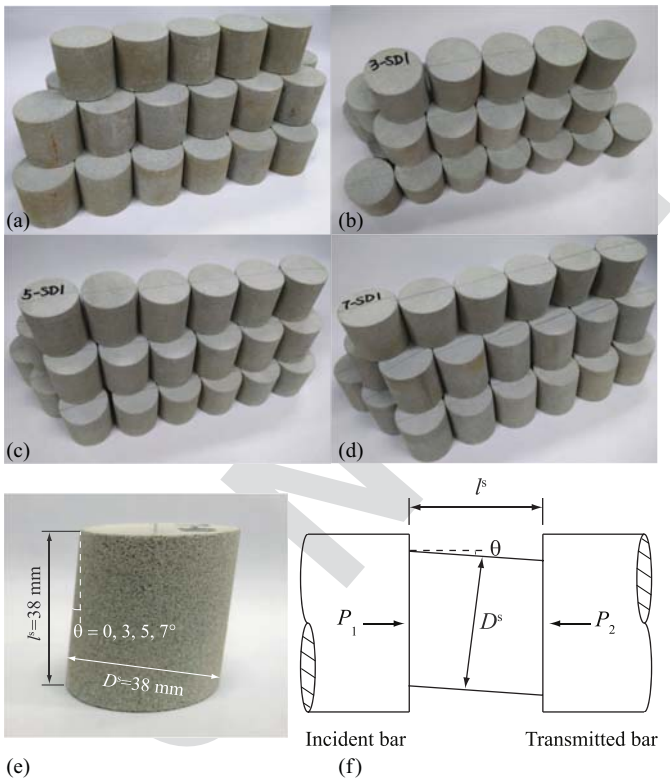

Fig. 1. Prepared specimens with a tilting angle of (a) 0°; (b) 3°; (c) 5°; and (d) 7°; (e) specimen geometry (D_s, θ and l_s are the diameter, the tilting angle, and the distance between the two parallel end surfaces, respectively); and (f) schematic of the specimen in SHPB testing.

(Neijiang, Sichuan province, China). The sandstone was homogeneous and isotropic in texture without visible discontinuities. Petrologic studies showed that the sandstone comprised feldspar (43%), quartz (35%), fragments (20%), and clay (2%), and the mineral size ranges from 200 to 300 μm (Du et al. 2020). Quasi-static unconfined compression tests were conducted on specimens with a slenderness ratio of 2:1 using a hydraulic servo controlled MTS815 testing system at Sichuan University to measure typical mechanical properties at a loading rate 0.56 MPa/s, including Young's modulus 8.0 GPa, Poisson's ratio 0.23, and uniaxial compressive strength 70 MPa. The overall density was measured as 2,320 kg/m^3.

A total of 160 sandstone specimens were prepared for the axially constrained dynamic compression-shear tests [Figs. 1(a–d)]. As shown in Fig. 1(e), the inclined cylinder specimen had a nominal diameter D_s of 38 mm from core drilling. The same set of the tilting angle θ of 0°, 3°, 5°, and 7° was considered in the experimentation herein, as in the previous study on the dynamic compression-shear loading without confinement (Xu and Dai 2018), in order to allow direct comparison of different axial preloads. The specimen length l_s, defined as the distance between two parallel loading surfaces, was chosen as 38 mm in order to satisfy the slender ratio of 1.0 for rock dynamic compression tests suggested by the International Society for Rock Mechanics (ISRM) (Zhou et al. 2012). Both ends of the specimens are carefully polished while guaranteeing the parallelism within 8′.

Experiment Setup

Tests were conducted using a modified SHPB system with an axial confining unit. This testing system essentially consists of a striker bar, an incident bar, and a transmitted bar with a specimen

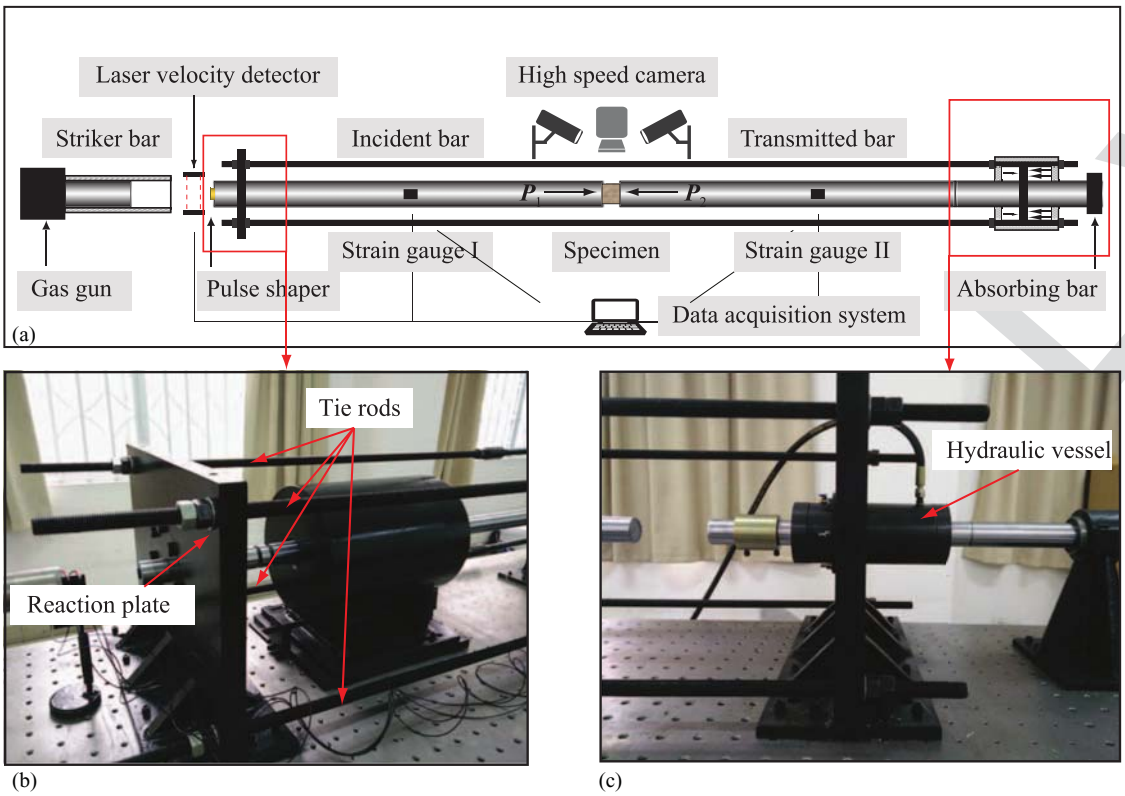

F2:1 **Fig. 2.** The axially constrained SHPB system: (a) schematic (not to scale); and (b and c) the axial confining system.

sandwiched in between, a data acquisition system, and additionally the axial confining system [Fig. 2(a)]. The striker is powered by a gas gun and then travels along a barrier before impacting upon the incident bar. A pair of rubber-copper stacked discs each with a dimension of 10 × 2 mm (diameter × thickness) is placed at the free end of the incident bar as a pulse shaper to reduce high-frequency oscillations of the incident wave and the dispersion effects (Gama et al. 2004; Dai et al. 2010). The incident bar and the transmitted bar are supported by multiple ball bearing supporters to allow free sliding and rotating about their axis and to reduce sagging. The free end of the transmitted bar is equipped with a hydraulic actuator [Fig. 2(c)] that is connected further to a reaction plate [Fig. 2(b)] near the impinge end of the incident bar via four tie rods. The tie-rod framework enables the initial axial hydraulic load applied to the bars between the actuator and the reaction plate, and it prevents potential buckling of the bars under compressive axial load.

The modified SHPB system is built up at State Key Laboratory of Hydraulics and Mountain River Engineering, Sichuan University, and dedicated for high-rate tests on rock-like materials. The diameter of the striker bar, incident bar, and transmitted bar is 50 mm to accommodate the mechanically representative dimension of the geomaterial bulk (Armstrong 1961, 2001), and the length is 300, 3,000, 2,000 mm, respectively. All bars are made from low-alloy ultrahigh strength steel, with a Young's modulus of 211 GPa and density of 7,800 kg/m^3. The incident and the transmitted bars are equipped with resistive strain gauges at appropriate positions to allow direct measurement of wave signals without superposition. Particular attention was additionally paid to the strain gauge on the incident bar to avoid the interference of a detachment wave in the measurement, which was due to the relaxation and the subsequent resumption of the axial preload during the incident pulse propagation (Chen et al. 2018). The hydraulic vessel provides an axial preload up to 78 KN.

Once a constant prestress state of the specimen is achieved under the initial preload (σ_{pre}), the striker is launched and impacts on the free end of the incident bar. With the pulse shaper tailoring the stress wave upon the impinge, a ramped nondispersive incident wave is generated and propagates toward the specimen, which partially transmits through and then travels along the transmitted bar and partially reflects back. The recorded strain signals of the so-called incident wave (ϵ_i), reflected wave (ϵ_r), and transmitted wave (ϵ_t) can be analyzed using one-dimensional stress wave theory based on the D'Alembert solution to calculate the mechanical response of the specimen as

$$P_1 = AE(\varepsilon_i + \varepsilon_r) + A\sigma_{\text{pre}}$$
$$P_2 = AE\varepsilon_t + A\sigma_{\text{pre}} \quad (1)$$

where P_1 and P_2 = forces imposed on the incident and transmitted ends of the specimen, respectively; and A and E = cross-section area and Young's modulus of the bar, respectively. More details of the operation of the axially constrained dynamic testing system and the data processing method can be found in previous work (Xu et al. 2020).

In order to unravel the coupling effect of the loading rate, the axial preload, and the combined compression-shear, a cross combination of these three factors was implemented. Eight grades were considered in the stress rate range from 500 to 4,000 GPa/s to cover typical damage levels of the sandstone specimen from unbroken-splitting transition to pulverization (Xu and Dai 2018). A preload ratio ∅ that described the relative magnitude of the axial confining pressure p with respect to the static compressive strength σ_c^s of Neijiang sandstone was defined to characterize the preload level as

$$\varnothing = \frac{p}{\sigma_c^s} \quad (2)$$

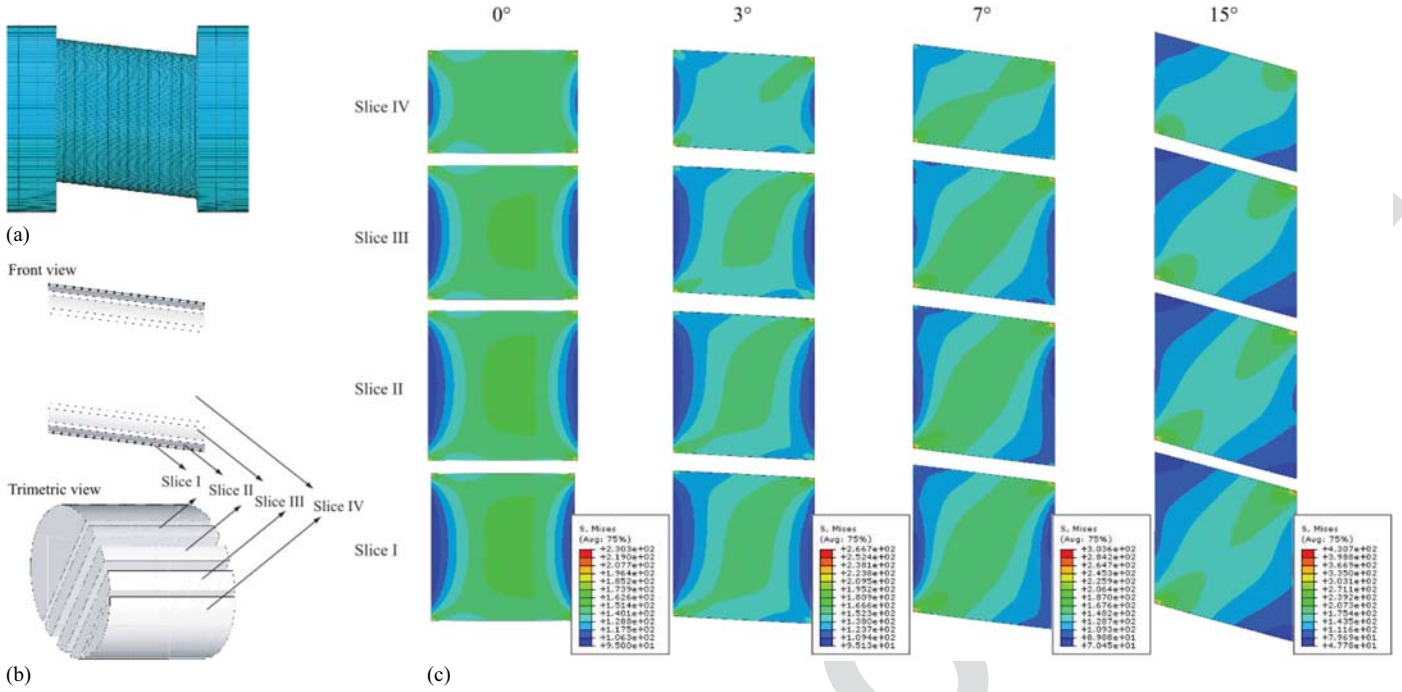

F3:1 F3:2 **Fig. 3.** (a) An example of the FEM model (partially shown) – a 7° specimen sandwiched between the incident bar (on the right) and the transmitted bar; (b) slicing strategy; and (c) equivalent stress distribution of 0°, 3°, 7°, and 15° specimens.

Five levels of the preload ratio were chosen from 0.1 to 0.9 with a step of 0.2, before which a preliminary set for variable-controlling tests were conducted under an approximately identical loading rate but different preload ratios ranging from 0.1 to 0.9 with a smaller step of 0.1. The achieved absolute axial precompression on specimens ranged from 7 to 63 MPa. Such a stress range covered the extreme in situ stress conditions that had been encountered in major underground rock engineering projects, for instance, Houziyan (Li et al. 2019), Baihetan (Dai et al. 2016a), and Wudongde (Li et al. 2018) hydropower stations in southwest China, whose maximum principal stress was measured as 22–36, 19–23, and 12–16 MPa, respectively. Distinct combinations of the compression-shear loads produced by the specimen inclination of 0°, 3°, 5°, and 7° were considered. The variance of the combined stress state and the mechanical characterization and approximation are elaborated in the next section.

Data Reduction Method

Stress and strain uniformity are critical for material characterization. Practically in lab-scale experimentation, however, the assumption of homogeneous stress or strain field is questionable even for simple specimen configurations (Pierron and Grédiac 2012). Complex geometry inevitably induces stress or strain singularity. In this respect, some compromises are made without losing uniformity at the critical material point. The Brazilian disk test (Fairbairn and Ulm 2002) is a classic example for characterizing brittle materials whose tensile strength is much less than its compressive counterpart, which is also the ISRM suggested method for characterizing the dynamic tensile strength of rock materials (Zhou et al. 2012). The Brazilian disk test is valid as long as cracking and failure initiate from the critical zone where homogeneity of the tensile stress is achieved, even though the biaxial stress state varies along the diametrical loading direction. This concept has been applied to studies involving the complex stress state (Dorogoy and Rittel 2005a, b). By analogy, the validity of the inclined specimen for material characterization under compression-shear loads has been addressed in previous work (Xu et al. 2020) by means of finite-element method (FEM) and DEM, regarding the dynamic equilibrium, stress uniformity, and interfacial friction effects. Critically, a high degree of stress homogeneity within the material failure area was verified. An approximation of von Mises equivalent stress and strain from the far-field measurement of a 7°-inclined specimen was subsequently established.

The same strategy was employed herein to approximate the equivalent stress and hydrostatic stress at the material failure point/area from the far-field nominal compressive stress $\widehat{\sigma_c}$. A commercial code ABAQUS was utilized to implement the FEM analysis. The numerical model of 0°, 3°, 7°, and 15° specimens in conventional SHPB testing was set up as shown in Fig. 3(a), driven by a nondispersive ramped wave measured from experiments. The material behavior is simplified as linear elastic with sufficient strength since its prepeak elastic behavior is of interest in the FEM simulations. The normal behavior of the bar-specimen contact is assumed to be hard, while the tangential behavior considers the interfacial friction. Parameters and material properties of the FEM model are detailed in Table 1. The distribution of the equivalent stress on four slices [Fig. 3(b)], which were equally spaced within half of the specimen and parallel to the maximum inclined section, are presented in Fig. 3(c). Homogeneous stress distribution was roughly achieved across the short diagonal of the inclined specimens, apart from the local stress concentration near the obtuse corners. The stress variance along this preferential failure path was quantified in Figs. 4(a and b). The equivalent stress σ_e and the hydrostatic stress σ_0 were further averaged by the path length s as $\widehat{\sigma_e}$ and $\widehat{\sigma_0}$, respectively, in the following to characterize the stress level and its uniformity:

$$\widehat{\sigma_e} = \frac{1}{s}\int_s \sigma_e ds \tag{3a}$$

$$\widehat{\sigma_0} = \frac{1}{s}\int_s \sigma_0 ds \tag{3b}$$

Although the stress distribution tended to be less homogeneous as the inclination increased, most of the area along the path experienced stress variation within 5% when the tilting angle was no more than 7°. Subsequently, the averaged equivalent stress $\widehat{\sigma_e}$ and hydrostatic stress $\widehat{\sigma_0}$ can be correlated with the nominal compressive stress $\widehat{\sigma_c}$ via linear regression [Fig. 4(c)] as

$$\widehat{\sigma_e} = f(\theta)\,\widehat{\sigma_c} \tag{4a}$$

$$\widehat{\sigma_0} = g(\theta)\,\widehat{\sigma_c} \tag{4b}$$

$$\widehat{\sigma_c} = P/A_s \tag{4c}$$

where P = far-field load on the specimen; and A_s = contact area of the bar–specimen interface. The coefficients $f(\theta)$ and $g(\theta)$, determined by specimen geometries, can be approximated as follows provided the FEM simulated results of the tilting angles under investigation:

$$f(\theta) = 0.98984 + 0.91597\ \tan(\theta) \tag{5a}$$

$$g(\theta) = 0.35742 + 0.45241\ \tan(\theta) \tag{5b}$$

The inclination is normalized by trigonometric function tangent to reflect the effect of the shear stress component.

Given dynamic equilibrium, Eq. (4) is valid in a range of loading regimes including the combined static-dynamic loading since the rule of linear superposition applies to the preload and the dynamic counterparts (Xu et al. 2020). The averaged equivalent stress $\widehat{\sigma_e}$ was employed to characterize the complex stress state of the inclined specimen and to allow direct comparisons among different combinations of the compressive and shear loads. The loading rate $\dot{\sigma}_e$ was defined as the slope of the linear prepeak portion of the time-varying $\widehat{\sigma_e}(t)$, while the failure strength the peak value. Depending on whether the preload is counted, the failure strength can refer to the dynamic strength, that is, the resistance of a preloaded sample to further dynamic loads, or total strength, that is, the overall capacity of the sample subjected to combined static-dynamic loads. The hydrostatic stress $\widehat{\sigma_0}$ contributed to depicting the failure envelope in deviatoric versus hydrostatic stress space. The FEM analysis also shows that the lateral confining pressure is significantly small with respect to the equivalent stress and the hydrostatic stress. This is because the bar–specimen interfaces are well lubricated thanks to the negligible interfacial friction effects on characterizing the stress and strain of interest (Xu et al. 2020). Hence, the friction-induced confining effects is significantly minimized and thus neglected in this study.

Table 1. Parameters and material properties of the FEM model

	Specimen	Bar
Constitutive model	Linear elasticity	Linear elasticity
Density (kg/m^3)	2,320	7,800
Young's modulus (GPa)	8	211
Poisson's ratio	0.23	0.33
Element type	C3D8R	C3D8R
Number of elements	337,218 (0° specimen) 348,254 (3° specimen) 317,268 (7° specimen) 374,400 (15° specimen)	588,027 (incident bar) 392,018 (transmitted bar)

Experimental Results

Dynamic Force Equilibrium

The dynamic force equilibrium of the specimens was checked in order to assess the validity of the high loading rate test prior to further data interpretation. Fig. 5 displays the time histories of the force on specimens of four tilting angles at different static-dynamic loading conditions. The incident wave, reflected wave, and transmitted wave recorded on the bars were superposed onto their associated baselines due to the preload and its relaxation and resumption, and they then shifted to the corresponding specimen–bar interfaces. The dynamic force on the incident side of the specimen was the sum of the incident and reflected waves, while the force on the transmitted side directly the transmitted wave [Eq. (1)]. A good agreement of the forces on both ends of the specimen was observed, despite the small discrepancy during the early loading stage in a few cases. Dynamic equilibrium was satisfied, especially during the steady rising of loading force until the peak force, which was the critical dynamic loading process related to the loading rate and the collapse strength of the specimen, respectively. We conclude that the stress measurement of the inclined specimens in the axially constrained high-rate tests

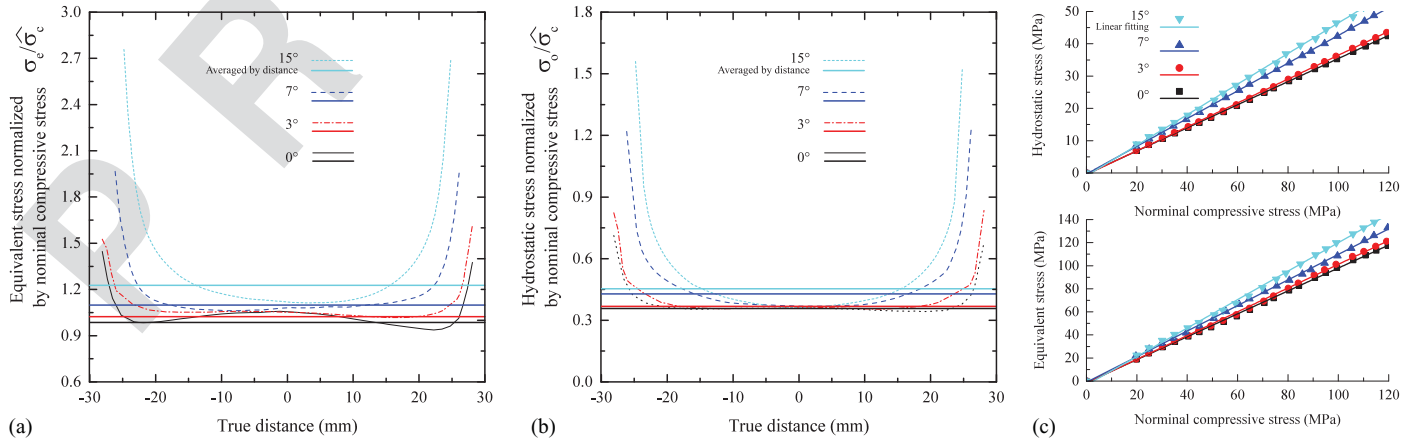

Fig. 4. Stress distribution along the preferential failure path: (a) equivalent stress; (b) hydrostatic stress; and (c) least-squares linear approximation of the averaged equivalent stress and hydrostatic stress from the nominal compressive stress.

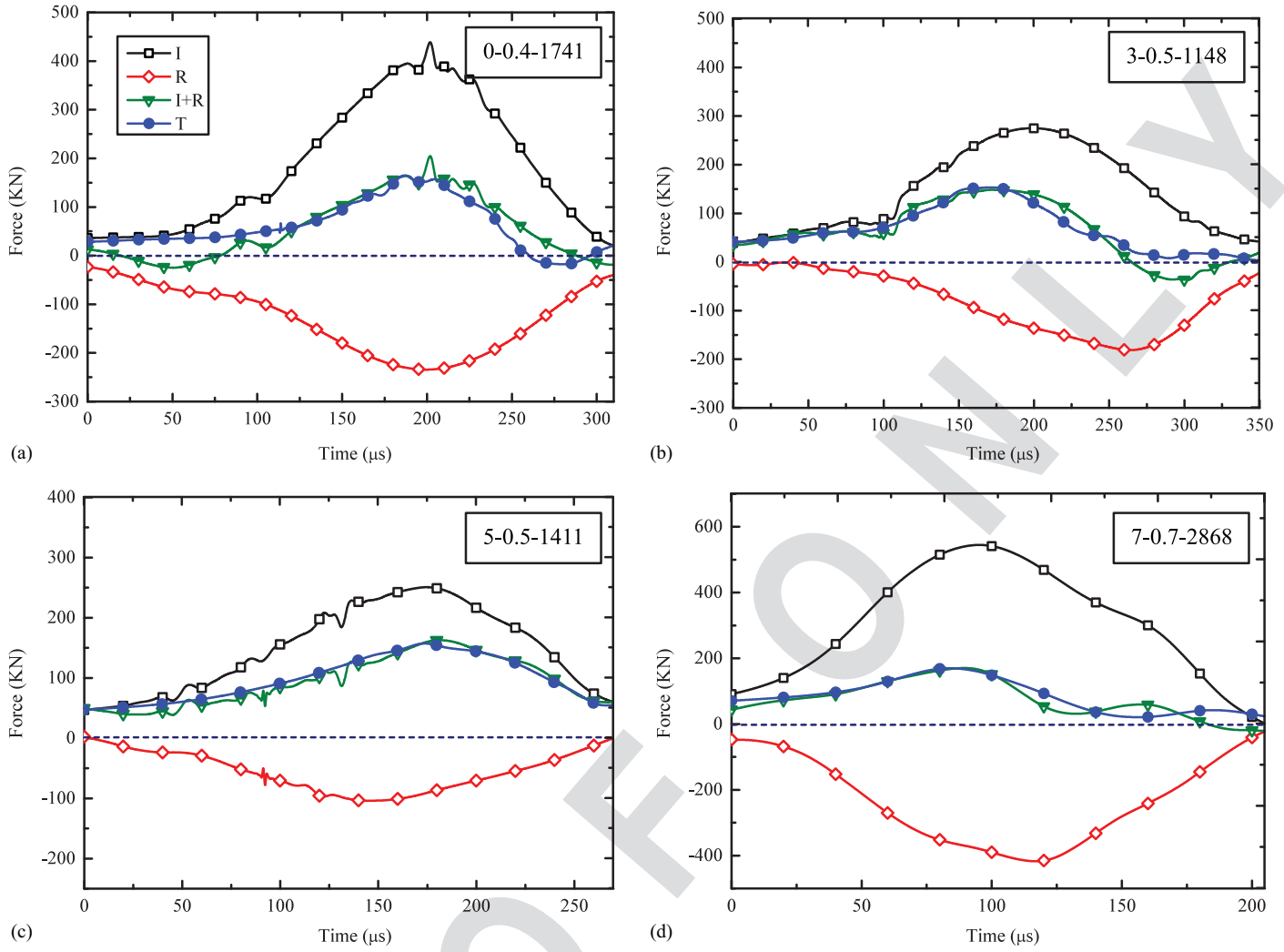

F5:1 **Fig. 5.** Dynamic forces on both ends of the specimens with a tilting angle of (a) 0°; (b) 3°; (c) 5°; and (d) 7°. Curves I, R, and T represent the incident,
F5:2 reflected, and transmitted waves, respectively. Legend 0–0.4–1,741 denotes the test on a 0° specimen, at a preload ratio of 0.4 and a loading rate of
F5:3 1,741 GPa/s.

and the processing method proposed are valid by virtue of pulse-shaping techniques.

Failure Strength and Envelope

Representative equivalent stress time histories of the specimens with four inclinations in the axially constrained SHPB tests are presented in Figs. 6 and 7. Results of 7° specimens are retrieved from the previous study (Xu et al. 2020). An identical preload is reached for each specimen geometry in Fig. 6 to reveal the rate sensitivity, whereas the dynamic load is approximately fixed in Fig. 7 to highlight the effect of the axial constraint. The response of the sandstone under axially constrained impact consists of the initial steady preloading state and the subsequent dynamic loading upon the arrival of the stress wave that included the linear growth, nonlinear variation, and stress peak followed by the catastrophic failure. Positive dependence of the equivalent stress on the imposed loading rate can be observed at any preload level under investigation (Fig. 6). The axial preload, however, has a more complicated effect on the failure strength and the loading rate (Fig. 7). As the preload increases, the failure strength rises markedly and then experiences a certain stress drop or plateau at a preload ratio around 0.7. A slight decrease of the loading rate is also associated with the increasing preload, indicating material deterioration induced by the axial preload.

A summary of the dependence of the failure strength on the imposed loading rate and the axial preload is given in Figs. 8 and 9 and Tables 2–4. Results of the unconstrained dynamic compression-shear tests (Xu and Dai 2018) and the axially constrained dynamic tests on 7° specimens (Xu et al. 2020) were retrieved from previous work and included to allow for a comprehensive comparison of the effects of the loading rate and the preload. Fig. 8 shows the approximately linear rate dependence of the dynamic equivalent strength, which is also influenced by the preload as indicated by the more pronounced rate sensitivity with the higher preload. Furthermore, material deterioration induced by the preload is clearly demonstrated by the dynamic equivalent strength decreasing with the increasing preload. Fig. 9 depicts the linear dependence of the total equivalent strength positively on the loading rate, which is, however, insensitive to the preload. Nonmonotonic enhancement of the total strength can be observed as the preload increased. The maximum total strength appears at a preload ratio around 0.7, followed by a plateau or a slight decrease with the increasing preload. Comparison with existing studies on the combined static-dynamic behavior of rock (Li et al. 2008) indicates that this turning point varies with rock materials and might be

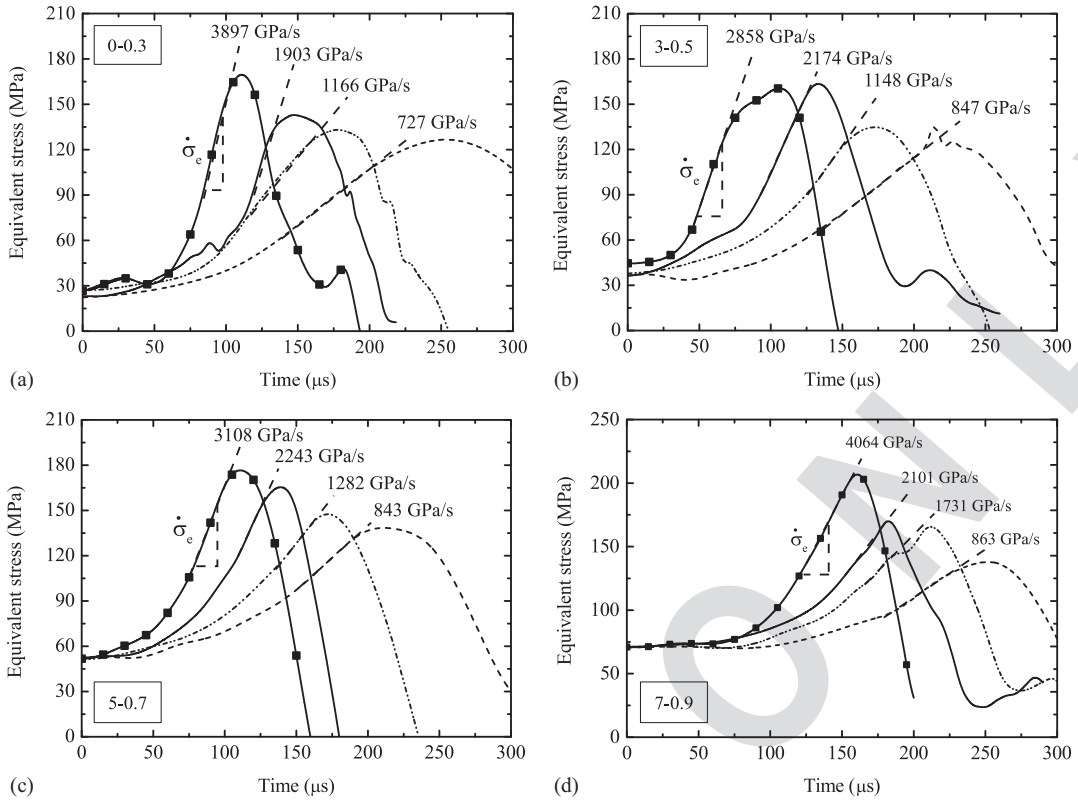

F6:1 F6:2 **Fig. 6.** Equivalent stress histories of (a) 0°; (b) 3°; (c) 5°; and (d) 7° specimens under different loading rates. Legend 0–0.3 denotes the test on a 0° specimen at a preload ratio of 0.3.

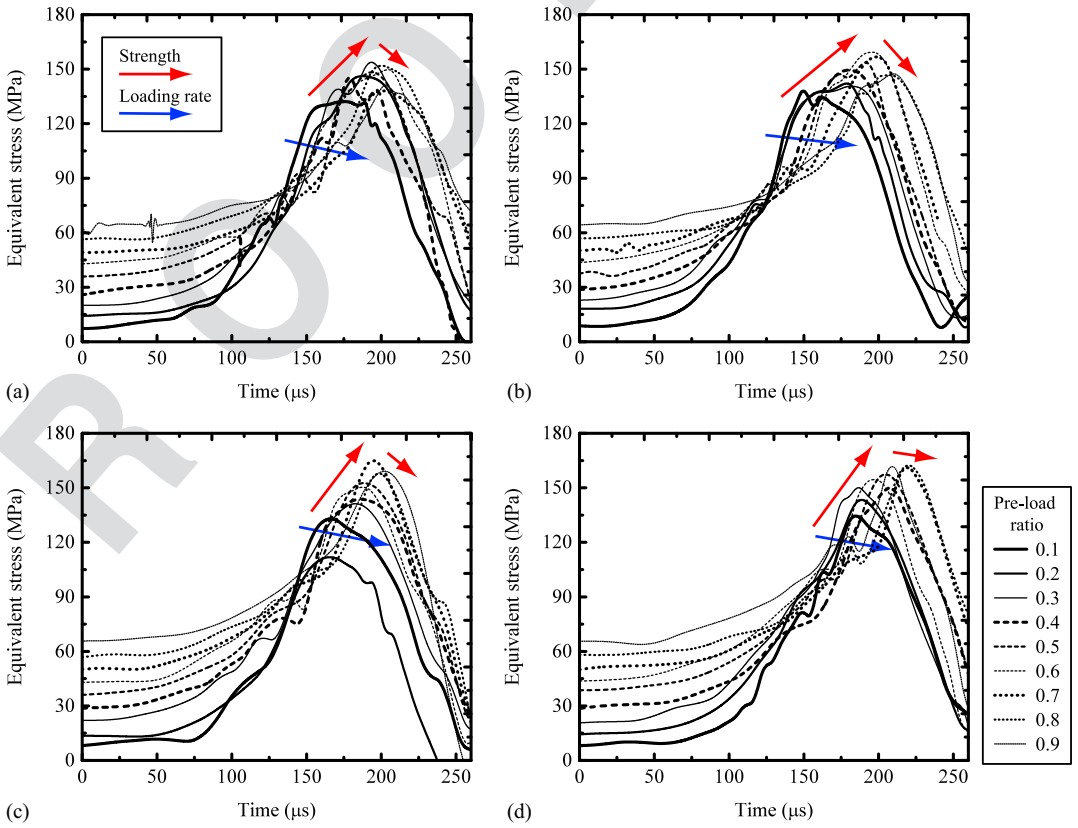

F7:1 F7:2 **Fig. 7.** Equivalent stress histories of (a) 0°; (b) 3°; (c) 5°; and (d) 7° specimens at varied preloads. The identical dynamic load was approximately achieved at an impact velocity of approximately 10 m/s.

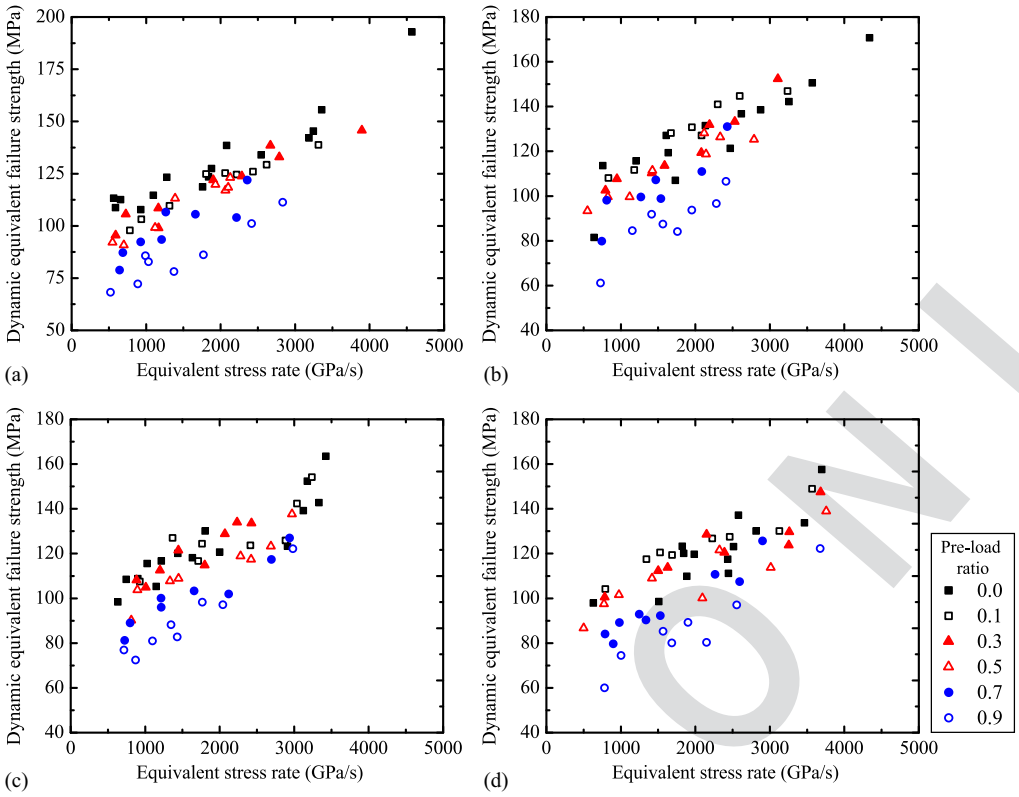

F8:1 **Fig. 8.** Rate dependence of the dynamic strength of (a) 0°; (b) 3°; (c) 5°; and (d) 7° specimens under varied preloads.

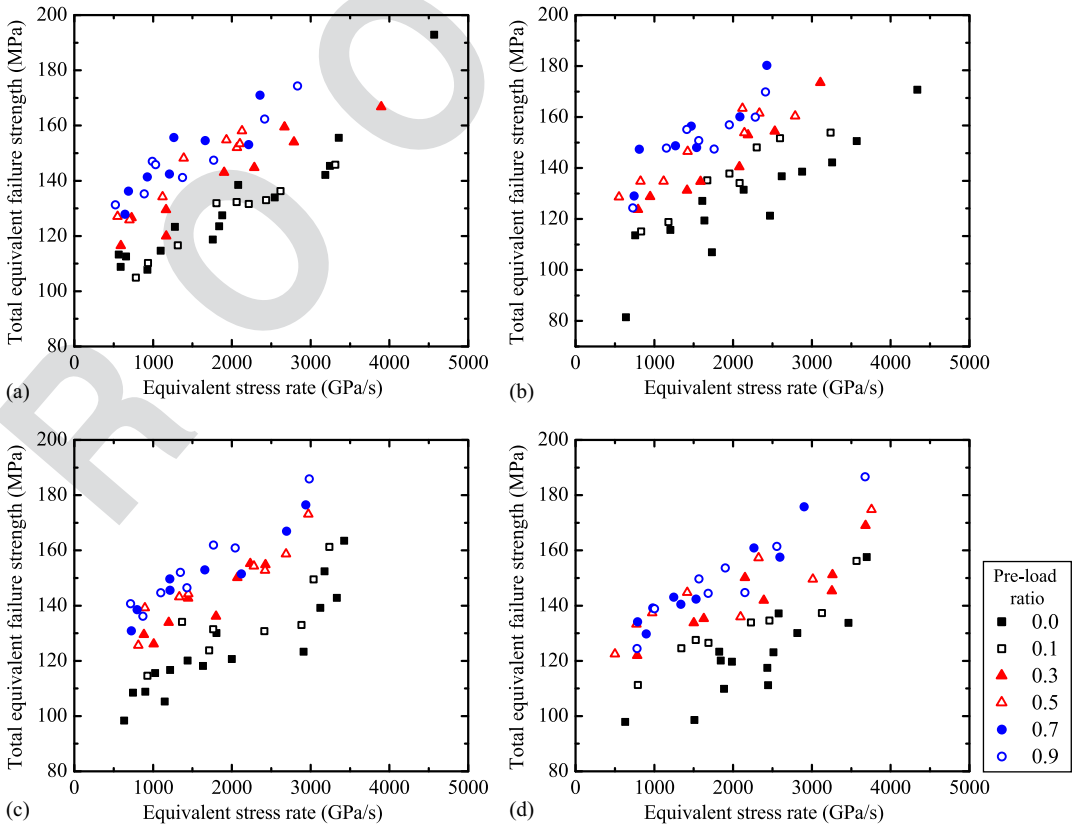

F9:1 **Fig. 9.** Rate dependence of the total strength of (a) 0°; (b) 3°; (c) 5°; and (d) 7° specimens under varied preloads.

Table 2. Strength of 0° specimens under combined static-dynamic loading

Specimen no.	Preload MPa (/UCS)	Equivalent stress rate GPa/s	Equivalent strength: Dynamic MPa	Equivalent strength: Total MPa
0-D11	0	565	112.5	112.5
0-D9		589	108.0	108.0
0-D10		657	111.8	111.8
0-D12		928	107.0	107.0
0-D4		1,097	113.9	113.9
0-D2		1,276	122.4	122.4
0-D3		1,758	117.9	117.9
0-D14		1,838	122.6	122.6
0-D7		1,878	126.6	126.6
0-D8		2,081	137.5	137.5
0-D5		2,544	133.0	133.0
0-D13		3,187	141.1	141.1
0-D15		3,245	144.4	144.4
0-D1		3,357	154.5	154.5
0-D6		4,568	191.5	191.5
0-SD37	7 (0.1)	782	97.2	104.2
0-SD11		934	102.5	109.4
0-SD16		1,314	108.8	115.8
0-SD9		1,804	124.0	131.0
0-SD20		2,060	124.4	131.4
0-SD42		2,215	123.7	130.7
0-SD33		2,435	125.1	132.1
0-SD27		2,616	128.4	135.3
0-SD47		3,312	161.0	144.8
0-SD12	21 (0.3)	592	94.8	115.7
0-SD38		727	104.8	125.7
0-SD25		1,054	107.7	128.6
0-SD18		1,166	98.3	119.1
0-SD30		1,903	121.1	142.0
0-SD43		2,285	122.9	143.8
0-SD32		2,669	137.5	158.4
0-SD4		2,789	132.1	152.9
0-SD48		3,897	144.8	165.6
0-SD13	35 (0.5)	550	91.4	126.2
0-SD39		701	90.2	124.9
0-SD19		1,120	98.5	133.2
0-SD6		1,389	112.4	147.1
0-SD21		1,930	118.9	153.7
0-SD31		2,065	116.2	150.9
0-SD44		2,103	117.6	152.3
0-SD35		2,129	122.2	157.0
0-SD40	49 (0.7)	643	78.3	127.0
0-SD15		686	86.7	135.3
0-SD22		925	91.7	140.4
0-SD26		1,206	92.8	141.5
0-SD7		1,262	105.9	154.6
0-SD37		1,660	104.8	153.5
0-SD28		2,213	103.4	152.0
0-SD45		2,356	121.1	169.8
0-SD41	63 (0.9)	519	67.8	130.4
0-SD17		886	71.8	134.3
0-SD29		988	85.2	146.1
0-SD23		1,030	82.3	144.9
0-SD10		1,373	77.6	140.2
0-SD36		1,768	85.6	146.5
0-SD34		2,414	100.5	161.2
0-SD46		2,831	110.6	173.2

Table 3. Strength of 3° inclined specimens under combined static-dynamic loading

Specimen no.	Preload MPa (/UCS)	Equivalent stress rate GPa/s	Equivalent strength: Dynamic MPa	Equivalent strength: Total MPa
3-D8	0	656	83.5	83.5
3-D9		775	116.5	116.5
3-D4		1,235	118.6	118.6
3-D1		1,651	130.4	130.4
3-D10		1,678	122.5	122.5
3-D7		1,776	109.8	109.8
3-D12		2,190	134.9	134.9
3-D5		2,532	124.4	124.4
3-D3		2,683	140.4	140.4
3-D13		2,951	142.1	142.1
3-D6		3,341	145.8	145.8
3-D11		3,662	154.4	154.4
3-D2		4,449	175.1	175.1
3-SD36	7 (0.1)	853	110.8	118.0
3-SD10		1,208	114.6	121.8
3-SD21		1,716	131.5	138.7
3-SD1		2,002	134.1	141.3
3-SD18		2,136	130.4	137.6
3-SD26		2,360	144.6	151.8
3-SD40		2,663	148.4	155.6
3-SD31		3,321	150.7	157.9
3-SD39	21 (0.3)	814	105.1	126.8
3-SD11		971	110.5	132.1
3-SD16		1,452	113.1	134.7
3-SD22		1,627	116.5	138.1
3-SD3		2,133	122.5	144.1
3-SD32		2,245	135.2	156.8
3-SD27		2,595	136.8	158.4
3-SD41		3,187	156.3	178.0
3-SD12	35 (0.5)	565	95.8	131.8
3-SD13		847	102.2	138.2
3-SD23		1,148	102.2	138.2
3-SD17		1,459	114.2	150.3
3-SD28		2,174	131.5	167.6
3-SD5		2,198	121.7	157.8
3-SD33		2,393	129.7	165.7
3-SD42		2,858	128.5	164.6
3-SD38	49 (0.7)	762	81.9	132.3
3-SD14		828	100.7	151.2
3-SD19		1,298	102.2	152.6
3-SD7		1,506	110.1	160.6
3-SD24		1,575	101.4	151.9
3-SD29		2,138	113.8	164.3
3-SD34		2,489	134.5	185.0
3-SD37	63 (0.9)	743	62.7	127.6
3-SD20		1,182	86.8	151.7
3-SD25		1,446	94.3	159.2
3-SD15		1,602	89.8	154.7
3-SD9		1,804	86.4	151.3
3-SD30		2,001	96.2	161.1
3-SD44		2,339	99.2	164.1
3-SD35		2,471	109.4	174.3

associated with the elastic-to-plastic deformation of the material. In addition, the sensitivity of the equivalent strength to the loading rate and the preload is independent of the different combinations of the compression-shear loads. Further explanation of the effect of the preload on the failure strength and the loading rate will be given in the section "Progressive Failure Process," from the perspective of the evolution of microcracks.

We proceed to establish the approximation of the failure strength from the loading rate and the preload via least square

Table 4. Strength of 5° inclined specimens under combined static-dynamic loading

Specimen no.	Preload MPa (/UCS)	Equivalent stress rate GPa/s	Equivalent strength: Dynamic MPa	Equivalent strength: Total MPa
5-D8	0	669	104.1	104.1
5-D10		788	114.7	114.7
5-D13		952	115.1	115.1
5-D5		1,084	122.3	122.3
5-D12		1,213	111.4	111.4
5-D11		1,285	123.5	123.5
5-D9		1,521	127.0	127.0
5-D4		1,728	125.0	125.0
5-D3		1,910	137.7	137.7
5-D15		2,116	127.6	127.6
5-D7		3,080	130.4	130.4
5-D1		3,303	147.2	147.2
5-D14		3,361	161.2	161.2
5-D6		3,526	151.1	151.1
5-D2		3,624	173.0	173.0
5-SD36	7 (0.1)	981	113.7	121.2
5-SD15		1,447	134.4	141.9
5-SD10		1,810	123.5	131.0
5-SD21		1,864	131.6	139.1
5-SD26		2,551	130.9	138.3
5-SD1		3,050	133.2	140.7
5-SD31		3,214	150.7	158.1
5-SD40		3,424	163.2	170.7
5-SD11	21 (0.3)	934	114.5	137.0
5-SD16		1,066	111.0	133.4
5-SD17		1,267	119.2	141.7
5-SD3		1,529	128.5	151.0
5-SD22		1,904	121.4	143.9
5-SD27		2,191	136.3	158.8
5-SD41		2,363	141.8	164.2
5-SD32		2,566	141.3	163.8
5-SD37	35 (0.5)	859	95.4	132.9
5-SD12		948	109.8	147.2
5-SD18		1,411	114.1	151.5
5-SD23		1,531	115.2	152.7
5-SD5		2,413	125.7	163.2
5-SD28		2,563	124.2	161.7
5-SD33		2,843	130.4	167.9
5-SD42		3,144	145.6	183.1
5-SD38	49 (0.7)	764	86.0	138.5
5-SD13		843	94.3	146.7
5-SD24		1,282	105.9	158.4
5-SD19		1,283	101.6	154.1
5-SD29		1,751	109.5	161.9
5-SD34		2,243	107.9	160.3
5-SD7		2,848	124.2	176.7
5-SD43		3,108	134.4	186.8
5-SD14	63 (0.9)	754	81.4	148.8
5-SD39		918	76.7	144.1
5-SD20		1,158	85.7	153.1
5-SD33		1,423	93.4	160.8
5-SD25		1,511	87.6	155.0
5-SD30		1,866	104.0	171.4
5-SD9		2,160	102.8	170.2
5-SD44		3,154	129.3	196.7

optimization, as illustrated in Fig. 10. A robust algorithm Trust Region Reflective is utilized to implement the minimization (Branch et al. 1999). The approximation equation, by employing the logarithmic loading rate dependence, and its coupled effect with the axial prestress is proposed as

$$\frac{\sigma_{sd}}{\sigma_s} = e^{A\varnothing(\varnothing - B)}\left[1 + C\left(\log_{10}\frac{\dot{\sigma}_e}{\dot{\sigma}_s}\right)^D\right] \quad (6)$$

where the nominal total failure strength σ_{sd} is normalized by the quasi-static compressive strength σ_s of the sandstone, and the equivalent stress rate $\dot{\sigma}_e$ (GPa/s) by the quasi-static loading rate $\dot{\sigma}_s$; $\varnothing$ = preload ratio. A and B are constants that reflects the influence of the axial prestress, while C and D are related to the loading-rate dependence. Optimization convergence is achieved in all cases with a tolerance of 1×10^{-8} satisfied. The constants that minimize the cost function for the four inclined specimens are summarized in Table 5. Hence, the failure strength of sandstone under combined static-dynamic loading can be approximated via Eq. (6) and Table 5.

Given three typical loading rates of 1,000, 2,000, and 3,000 GPa/s associated with the specimen damage level of unbroken-splitting transition, fragmentation, and pulverization, the nominal compressive strength is approximated at a different preload ratio varying from 0.0 to 0.9. The equivalent stress and hydrostatic stress at failure point are then deduced from the interpolated compressive strength via Eqs. (4) and (5) and plotted as scatters in deviatoric versus hydrostatic stress space (Fig. 11) to assess the evolution of the combined static-dynamic failure envelope as the preload increases. Drucker–Prager (D–P) criterion (Drucker and Prager 1952; Alejano and Bobet 2012) is employed to construct the failure envelopes, shown as lines in Fig. 11, via least square optimization. Convergence of the cost minimization is satisfied in all cases at a tolerance of 1×10^{-8}. It can be seen that, given a loading rate, the D–P failure surface expands as the preload increases. The expansion approaches its upper bound when the preload ratio approximates 0.8. The extreme D–P failure surfaces at the three loading rates are $\widehat{\sigma_e} = 44.9 + 1.86\,\widehat{\sigma_o}$, $\widehat{\sigma_e} = 49.1 + 1.90\,\widehat{\sigma_o}$, and $\widehat{\sigma_e} = 46.8 + 2.01\,\widehat{\sigma_o}$, respectively. Apparent rate dependence of the failure envelope of the sandstone is also observed.

Failure Pattern

The axially constrained SHPB tests at a high loading rate around 3,000 GPa/s were instrumented with a Fastcam SA-Z high-speed digital camera in order to capture the progressive failure process of the four compression-shear specimens under combined static-dynamic loads. The camera was set at 160,000 frames per second with an average exposure time of 4.6 μs. Fig. 12 shows representative high-speed photographs depicting the crack evolution at a preload ratio of 0.7, since this preloading condition appears to be a critical point of the influence of the axial prestress on the failure strength and failure envelope. Five typical moments mark the arrival of the stress wave, crack initiation, crack growth, pervasive damage, and fragment detaching, respectively. Axial compression and lateral dilation were observed prior to random crack initiation within the specimen 40–60 μs after the arrival of the incident wave. The cracks in the 0° specimen subsequently grew along the axial loading direction, forming typical wing-cracks as expected for brittle materials in compression. By contrast, extensive bifurcation was discerned for the three inclined specimens, as both the global shear failure and the local tensile damage were happening. The local tensile cracks initiated along the core axis of the inclined specimen, while the global crack coalescence was predominated by the shear band oriented along the short diagonal. As a consequence, the inclined specimens were penetrated by a wide shear band where secondary tensile cracks largely developed. The detaching and popping of the resulted fragments helped to better identify

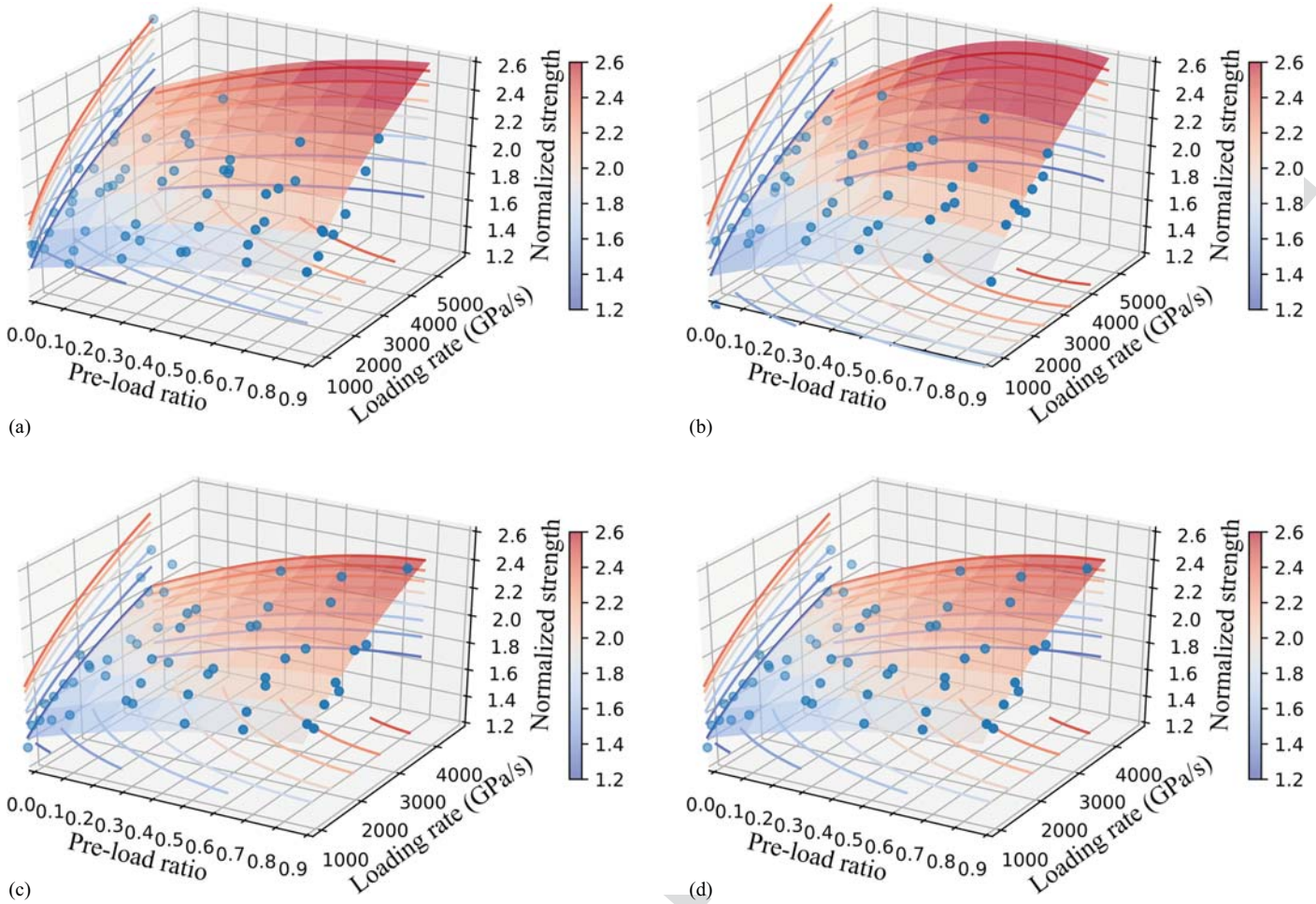

F10:1 **Fig. 10.** Approximation of the failure strength from the loading rate and the axial prestress.

Table 5. Constants of the approximation of the failure strength from the loading rate and preload

Parameters	0° specimen	3° specimen	5° specimen	7° specimen
A	−0.192	−0.436	−0.250	−0.419
B	2.141	1.495	1.983	1.544
C	1.29×10^{-06}	1.10×10^{-07}	8.26×10^{-07}	2.93×10^{-07}
D	7.121	8.394	7.314	7.762

the predominant failure pattern of the 0°, 3°, 5°, and 7° specimens as (1) axial wing-cracking, (2) double-S shear accompanied by pervasive bifurcation, (3) feather-like fracture band, and (4) twisted fracture band, respectively. It is concluded that the compression-shear specimen failed prevailingly by shear coupled with local tensile cracking in axially constrained SHPB testing at a preload ratio of 0.7.

A summary of the dynamic failure pattern of the compression-shear specimens under different preloading conditions is given in Fig. 13. At a given preload level, shear failure became more pronounced with the increasing inclination, as demonstrated by the axial splitting failure mode of 0° specimens in contrast to the diagonal shearing of 7° specimens. The influence of the axial constraint was more complex on the failure mode. For each inclined specimen, the higher preload induced the more local tensile damage as indicated by the pervasively growing secondary axial cracks, but the less shear failure as shown by the significantly reduced surface spalling and the smaller inclination of the shear fracture band. A consequence of the extensive local tensile fractures was a higher degree of fragmentation that would require more surface energy to generate cracks. On the other hand, this explained the positive dependence of the failure strength on the axial preload. An interesting phenomenon was observed at a low preload that the inclined specimen failed by axial or subaxial throughgoing fractures instead of a pronounced shear band that happened at high preloads. Possible explanations are further elaborated in the section "Progressive Failure Process," regarding the influence of the preload on the microstructures of the sandstone specimen.

DEM Modeling

Brief Description of DEM

The classical granular DEM model treats rock as an assembly of deformable particles that interact with each other at contact points by proper constitutive models of contact. The problem can be solved two ways. First, through iterations by updating the force and position of the varying contacts as

$$\boldsymbol{F}_{ij}^{n} = K_{ij}^{n}\boldsymbol{U}_{ij}^{n} \tag{7a}$$

$$\boldsymbol{F}_{ij}^{s} \leftarrow \boldsymbol{F}_{ij}^{s} + k_{ij}^{s}\Delta\boldsymbol{U}_{ij}^{s} \tag{7b}$$

where the normal force $\boldsymbol{F}_{ij}^{n}$ is related to the total relative normal displacement $\boldsymbol{U}_{ij}^{n}$ via the normal stiffness K_{ij}^{n} (secant stiffness); while the shear force $\boldsymbol{F}_{ij}^{s}$ is updated by the increment of shear

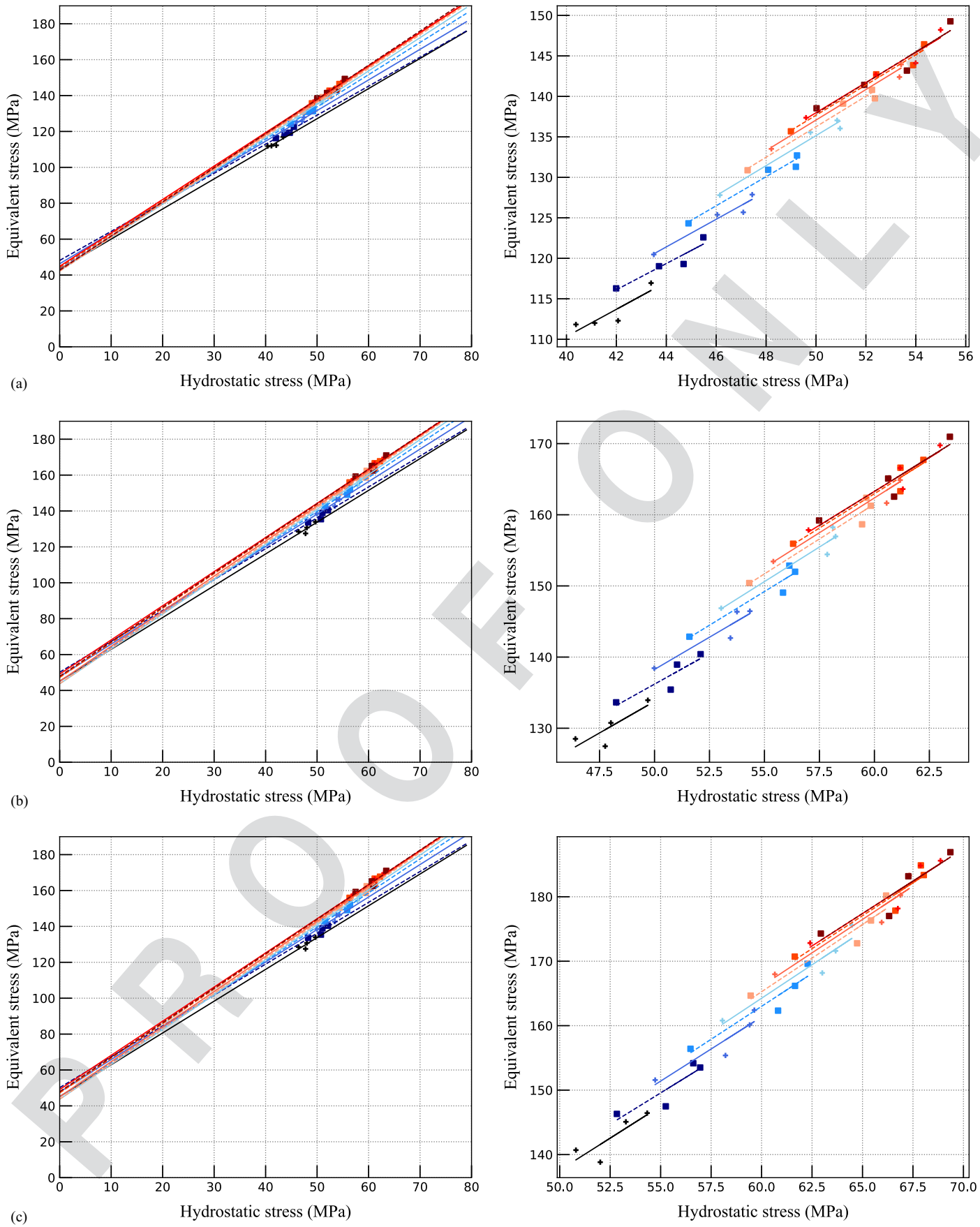

F11:1 **Fig. 11.** Failure envelopes of sandstone under combined static-dynamic loading at three typical loading rates: (a) 1,000 GPa/s; (b) 2,000 GPa/s; and
F11:2 (c) 3,000 GPa/s.

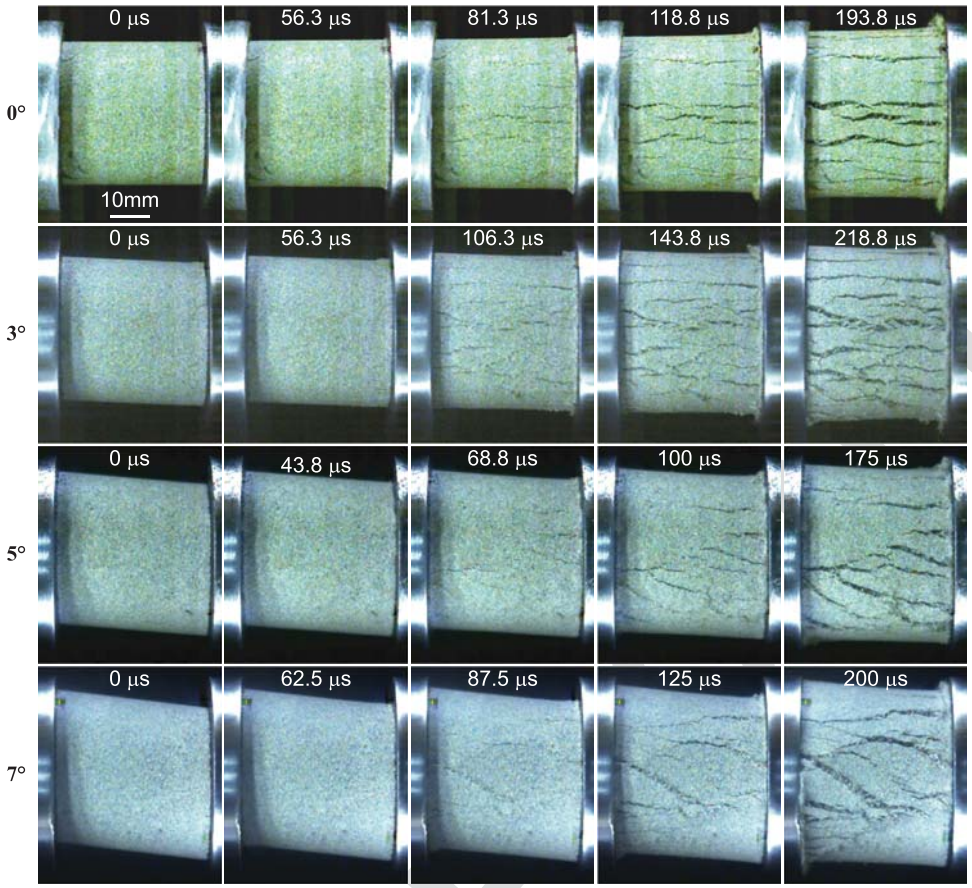

F12:1 **Fig. 12.** Progressive failure process of compression-shear specimens in axially constrained SHPB testing at a preload ratio of 0.7 and loading rate of
F12:2 approximately 3,000 GPa/s, demonstrated via high-speed photographs. The incident bar is on the right.

displacement $\Delta \boldsymbol{U}_{ij}^{s}$ via the shear stiffness k_{ij}^{s} (tangential stiffness). The subscript ij indicates the entity refers to the contact between the ith and jth particles.

Second, through integrating the equations of motion of the constituent structural units which are governed by Newton's second law as

$$\ddot{\boldsymbol{u}}_i = \frac{\boldsymbol{F}_i}{m_i} + \boldsymbol{g} \tag{8a}$$

$$\ddot{\boldsymbol{\theta}}_i = \frac{\boldsymbol{M}_i}{I_i} \tag{8b}$$

where $\ddot{\boldsymbol{u}}_i$ and $\ddot{\boldsymbol{\theta}}_i$ = translational and rotational accelerations, respectively. The resultant force $\boldsymbol{F}_i$ is calculated as the vectorial summation of all the forces on the ith particle $\boldsymbol{F}_i = \sum_j (\boldsymbol{F}_{ij}^{n} + \boldsymbol{F}_{ij}^{s}) + \boldsymbol{F}_i^{\text{ext}}$, and the resultant moment $\boldsymbol{M}_i$ the vectorial summation of all the moments $\boldsymbol{M}_i = \sum_j \boldsymbol{F}_{ij}^{s} r_{ij} + \boldsymbol{M}_i^{\text{ext}}$, where $\boldsymbol{F}_i^{\text{ext}}$ and $\boldsymbol{M}_i^{\text{ext}}$ = external force and moment acting on the ith particle, respectively; and r_{ij} = distance between contact point and the particle centroid.

As the most popular contact model for simulating intact rocks, the bonded-particle model (BPM) developed by Potyondy and Cundall (2004) approximates rock as a cemented granular material by introducing additional bond contacts between particles. The intergranular behavior is assumed to be perfectly brittle. A bond breaks if the local force and/or displacement meet a specified breakage criterion; for example, the maximum stress criterion, which can be represented as

$$\sigma_{\max} = -\frac{\boldsymbol{F}_k^{n}}{A_k} + \frac{|\boldsymbol{M}_k^{s}|}{I_k} R_k \geq \sigma_c \tag{9a}$$

$$\tau_{\max} = \frac{|\boldsymbol{F}_k^{s}|}{A_k} + \frac{|\boldsymbol{M}_k^{n}|}{J_k} R_k \geq \tau_c \tag{9b}$$

where $\sigma_{\max}$ and $\tau_{\max}$ = maximum tensile and shear stress of the kth bond, respectively; σ_c and τ_c = tensile and shear strength, respectively; and R_k, A_k, I_k, and J_k = radius, area, moment of inertia, and polar moment of inertia of the cross section of the bond disk, respectively. A cohesionless frictional sliding behavior is imposed following the bond breakage as

$$F_{\max}^{s} = \mu |\boldsymbol{F}_i^{n}| \tag{10a}$$

$$\boldsymbol{F}_i^{s} \leftarrow \frac{\boldsymbol{F}_i^{s}}{[\boldsymbol{F}_i^{s}]} F_{\max}^{s} \tag{10b}$$

The slip is allowed to occur if the shear force exceeds the maximum admissible shear contact force $F_{\max}^{s}$ that is related to the normal force via the friction coefficient μ.

Model Setup and Calibration

The open DEM source code ESyS-Particle (Weatherley et al. 2011; Zhao et al. 2015) was employed herein to investigate the fracturing mechanism of the prestressed inclined specimen subjected to dynamic loading. The three-dimensional model of specimens with an inclination of 0°, 7°, 15°, and 30° in SHPB testing were set up [Fig. 14(a)]. The synthetic specimen was created using a well-developed dense-packing method (Potyondy and Cundall 2004; Weatherley et al. 2011), and the bar model via a novel mirror-bonding method (Dai et al. 2016b) that was dedicated to creating

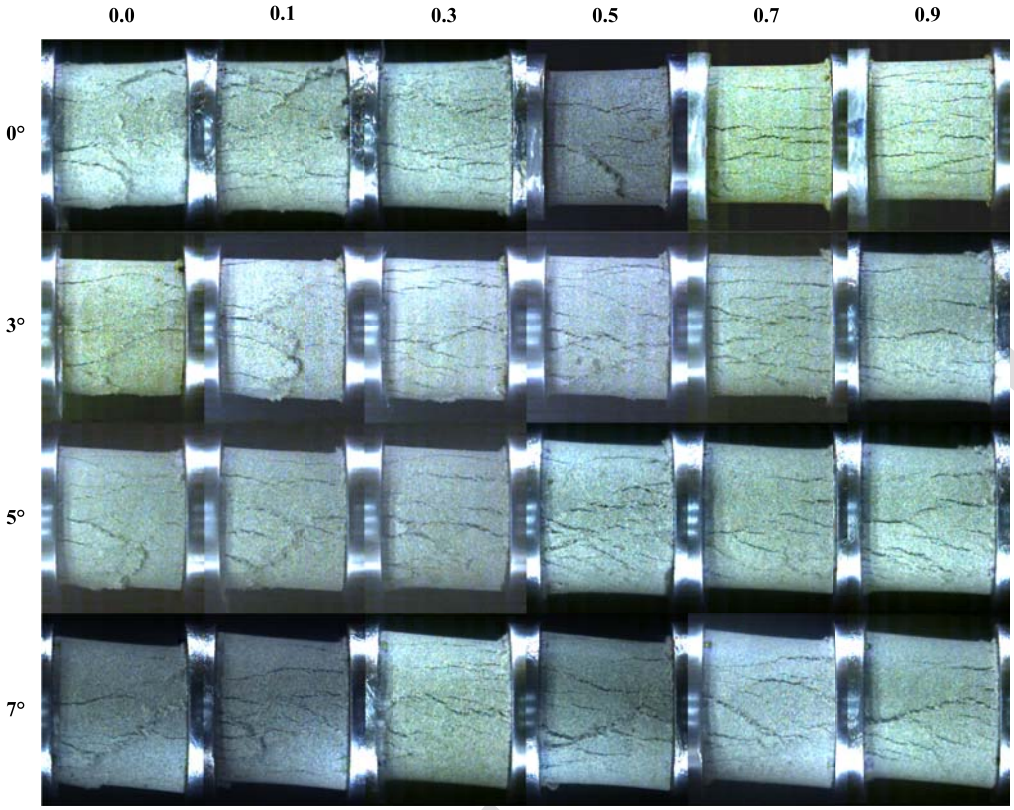

F13:1 **Fig. 13.** A collection of the failure pattern of compression-shear specimens under different preloading conditions, demonstrated via high-speed photographs. The loading rate approximates 3,000 GPa/s; the incident bar is on the right.
F13:2

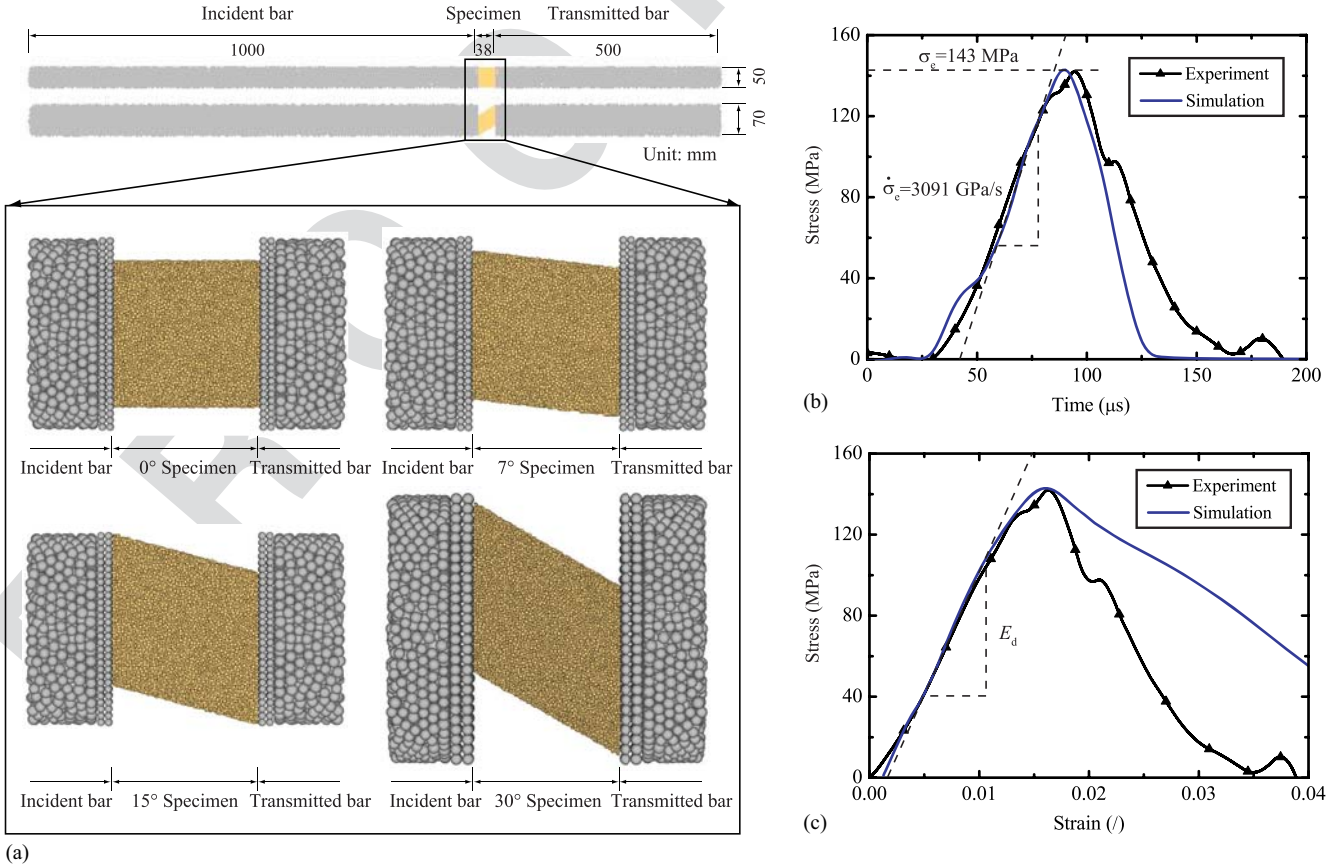

F14:1 **Fig. 14.** (a) DEM model setup; (b) calibration of the stress history; and (c) the stress–strain relationship of a 0° specimen.

compact solids of large slenderness ratio from randomly distributed particles. This method has been employed in numerical studies on SHPB testing of three-dimensional specimens such as cracked chevron-notched Brazilian disk (Dai et al. 2016b) and cylindrical specimen additionally subjected to hydrostatic confining pressure (Du et al. 2018). Valid stress wave propagation was recorded. Dynamic forces on both ends of the specimen deduced from the three-wave method matched those directly measured on the bar–specimen interface by tracking and summing the contact force vectors through the uniform layers of the particles between the bars and the specimen (Dai et al. 2016b). By virtue of this direct measuring method, the length of the numerical bars can be largely reduced while preventing stress wave superposition at the specimen boundaries. The simulation covers different combinations of the loading rate from 700 to 4,000 GPa/s at eight grades and the preload ratio from 0.0 to 0.9 at six levels.

A linear elastic bond model is employed as the constitutive model of the contact between particles, where the bond can resist normal and shear forces, as well as bending moments, in a linear elastic manner. The bond breakage is determined via the maximum stress criterion as described by Eq. (9), after which the cohesionless frictional sliding behavior [Eq. (10)] is activated. The microparameters of the DEM model were carefully calibrated via a trial-and-error method, according to the physical and mechanical properties of the sandstone specimen and the bars. For the sake of computational efficiency, the incident wave signal recorded from the experiment using the pulse-shaping techniques was explicitly applied on the boundary particles of the numerical incident bar to initiate the impact. Most importantly, the microscopic strength and stiffness of the bonds were precisely regulated by matching the stress histories and the stress–strain relationships of the model with the experimental measurements. A good agreement of the prepeak stress–time curves [Fig. 14(b)] indicates that the selected parameters can reasonably reproduce the dynamic failure strength at the loading rate determined by the incident stress wave; the consistency of the prepeak stress–strain curves [Fig. 14(c)] suggests that the dynamic Young's modulus and the failure strain of the sample can be well described. The calibrated microscopic parameters are summarized in Tables 6 and 7, which are consistent with those calibrated in the previous study on 7° specimens under combined dynamic loading (Xu et al. 2020).

The dynamic equilibrium of the inclined specimens under combined static-dynamic loading was assessed to validate the numerical simulations. Fig. 15 presents examples of the dynamic balance check under various loading regimes. The forces on the incident end F_I and on the transmitted end F_T of the specimen were measured as the vectorial summation of the contact forces between the respective bar-specimen interfacial particles. An equilibrium coefficient $\mu = ((F_I - F_T)/(F_I + F_T)/2)$ was defined to quantify the level of the dynamic balance. After a few wave reverberations inside the specimen during the early stage of the loading, the dynamic forces on the specimen boundaries started approaching each other. Meanwhile, the equilibrium coefficient oscillated within ±10% after the initial unbalance, indicating reasonable dynamic equilibrium was achieved throughout the dynamic loading process. It is noted that the preload does not adversely affect the dynamic equilibrium while the extremely high loading rate and inclination make it difficult to reach the balance. This is because either a high loading rate or a complex specimen geometry leads to insufficient wave reverberations to reach dynamic equilibrium before the failure of the rock specimen. Moreover, simulations demonstrated that the maximum compression load that the inclined specimen can sustain decreased with the inclination, which meant that the specimens with a large inclination would fail during the initial axial preloading. No further simulated results of 15° and 30° specimens are provided in the following sections.

Table 6. Calibrated microscopic parameters of the DEM model: specimen 15

Microscopic parameters	Particle	Bond	Sandstone	Model
Radius (mm)	0.33–0.55	—		
Density (kg/m^3)	3,569	—		
Young's modulus (GPa)	11	11		
Stiffness ratio k_n/k_s	2.5	2.5		
Friction coefficient	0.5	—		
Tensile strength σ (MPa)	—	58 ± 0		
Shear strength τ (MPa)	—	290 ± 0		
Macroscopic properties				
Density (Kg/m^3)			2,320	2,320
Young's modulus (GPa)			8	8.8
Poisson's ratio			0.23	0.25
Uniaxial compressive strength (MPa)			70	69.8

Table 7. Calibrated microscopic parameters of the DEM model: bar

Microscopic parameters	Particle	Bond	Steel	Model
Radius (mm)	1.50–1.67	—		
Density (kg/m^3)	12,000	—		
Young's modulus (GPa)	245	—		
Stiffness ratio k_n/k_s	3	—		
Friction coefficient	0.5	—		
Tensile strength σ (MPa)	—	1×10^{100}		
Shear strength τ (MPa)	—	1×10^{100}		
Macroscopic properties				
Density (kg/m^3)			7,800	7,800
Young's modulus (GPa)			211	211

Fragmentation

Following the calibration of the mechanical response of the inclined specimens at the macroscopic level, the DEM model was further verified by comparing the reproduced fragmentation with the experimental observation. A bond breakage tracking algorithm was employed to detect the distribution of the clustered particles, which were bonded internally but exhibited the frictional sliding behavior externally. These clusters thus represented the fragments at the macroscopic level. Fig. 16 shows the comparison between the fragmentation obtained from simulations and experiments of 0° and 7° specimens at a high loading rate around 3,000 GPa/s. In simulations, particles that constituted the same cluster were illustrated in an identical color, while those of the adjacent clusters were distinguished in different colors. In particular, particles in blue denoted orphans of which all the original bonds had broken, which represented the experimentally observed debris of the size within the submillimeter range. The corresponding experimental observations were focused on the specimen end that was retrieved from the postmortem examination, and the circumferential free surface that was captured via the high-speed camera (see section "Failure Pattern"). The prevailing fractures and fragments of 0° and 7° specimens are additionally sketched from the simulated and experimental results for a better comparison.

Fig. 16 demonstrates that the simulated fragmentation of 0° and 7° specimen was consistent with that observed in experiments at a high loading rate, with the effects of the preload being reflected.

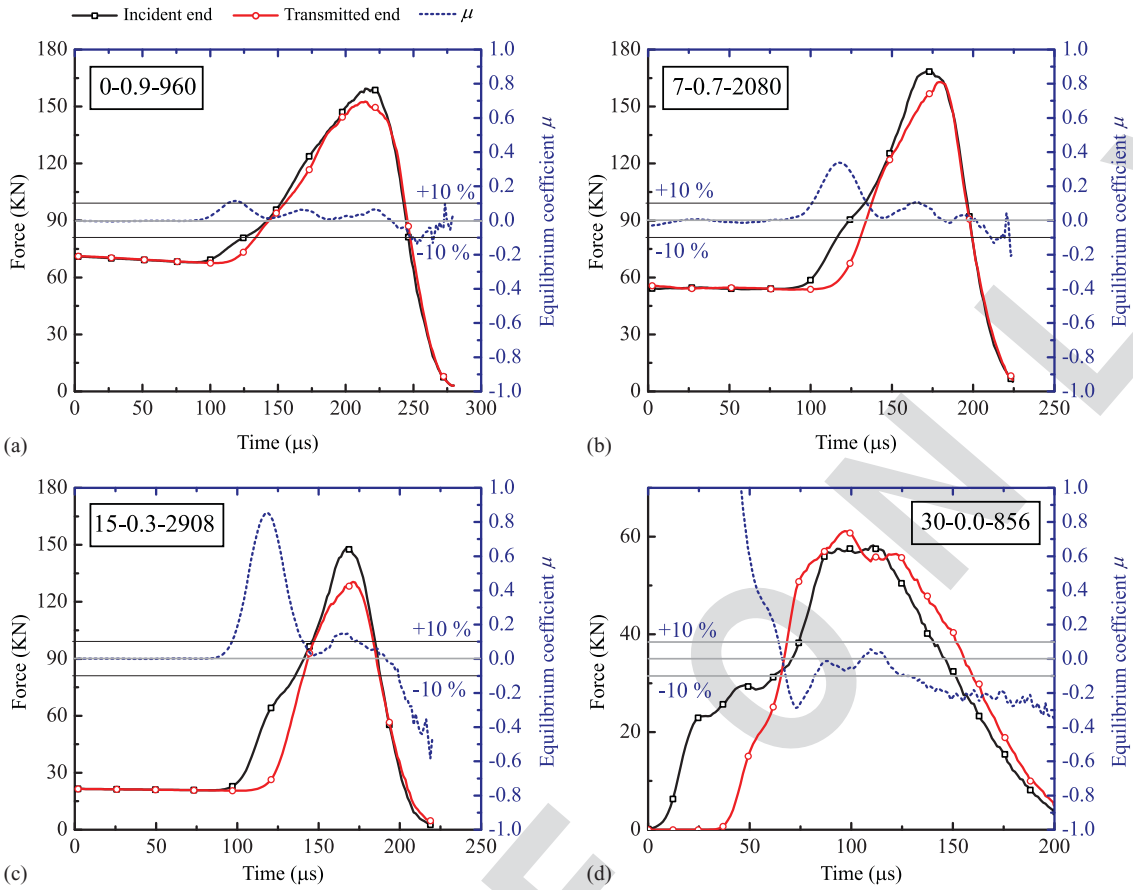

F15:1 **Fig. 15.** Dynamic force balance check of simulations: (a) 0°; (b) 7°; (c) 15°; and (d) 30° specimens under combined static-dynamic loading. Legend
F15:2 0–0.9–960 denotes 0° specimen, preload ratio of 0.9, and loading rate of 960 GPa/s.

As a joint result of radial cracks and circumferential cracks, the fragments at the 0° specimen end were distributed in a concentric rosette form, with its center fully pulverized. The axial fractures split the circumferential free surface into subparallel strips. As the preload increased, more strips were generated, indicating a higher degree of fragmentation. By contrast, an eccentric rosette-like distribution of fragments that deviated toward the obtuse corner was observed at the end of the 7° specimen. This was the result of the shear fracture band that came with the biaxial stress rate, splitting up the inclined specimen along its short diagonal. Note that the cracks along the long diagonal were bifurcated from the main fracture after the specimen failure near the loading end moment. The complex effects of the preload on the failure pattern were accurately reproduced in the simulations showing that the predominant failure pattern varied from the short-diagonal shear fracture under no preload, to subaxial splitting at a low preload, and to bifurcated shear band at a high preload. The higher preload was also characterized with a higher degree of fragmentation. Fig. 16 validates that the DEM model developed herein is capable of reproducing the hybrid effects of the combined compression-shear loads and the static-dynamic loads on the fragmentation of the sandstone specimens.

Progressive Failure Process

The validated DEM model was further exploited to assess the evolving internal damage of the opaque samples, which otherwise remained challenging in dynamic in-situ experiments. The progressive cracking process of 0° and 7° specimens under typical combined static-dynamic loading conditions are illustrated in Figs. 17 and 18, respectively. The three-dimensional spatial distribution of the microcracks was visualized by the four slices using the same slicing strategy as described in Fig. 3(b). The black boxes represent the maximum outline of these slices. Six characteristic moments from the macroscopic mechanical response were selected, including preloading t_{pre}, dynamic equilibrium t_b, linear–nonlinear transition deformation t_t, peak force t_p, 10% force drop after peak t_{p10}, and loading end t_e.

The evolving microcracks at these typical moments demonstrated the collective influence of the microstructural damage on the macroscopic behaviors. At t_{pre}, few microcracks had been initiated due to preloading. This agreed with the quasi-static behavior of the sandstone specimen where the linear–nonlinear transition point of the stress–strain relationship was very close to the failure point (Xu and Dai 2018). The insignificant damage cumulation before the nonelastic deformation of rocks has also been widely observed in the literature (Khazaei et al. 2015; Zhang et al. 2020). However, more microcracks initiated as the preload increased. An embryo of the final shear band that was later observed in inclined specimens had been depicted by the microcracks scattering on the short diagonal at the preload ratio of 0.9. At t_b, a few more microcracks formed on both ends of the specimen. The nearly equal amount of the microcracks on the either end indicated sufficient wave reverberations back and forth from the incident to the transmitted bar–specimen interfaces to achieve dynamic equilibrium. Furthermore, as the preload increased, very few microcracks initiated during t_{pre} to t_b of 0° and 7° specimens. This suggested that the preload might facilitate the dynamic equilibrium and agreed

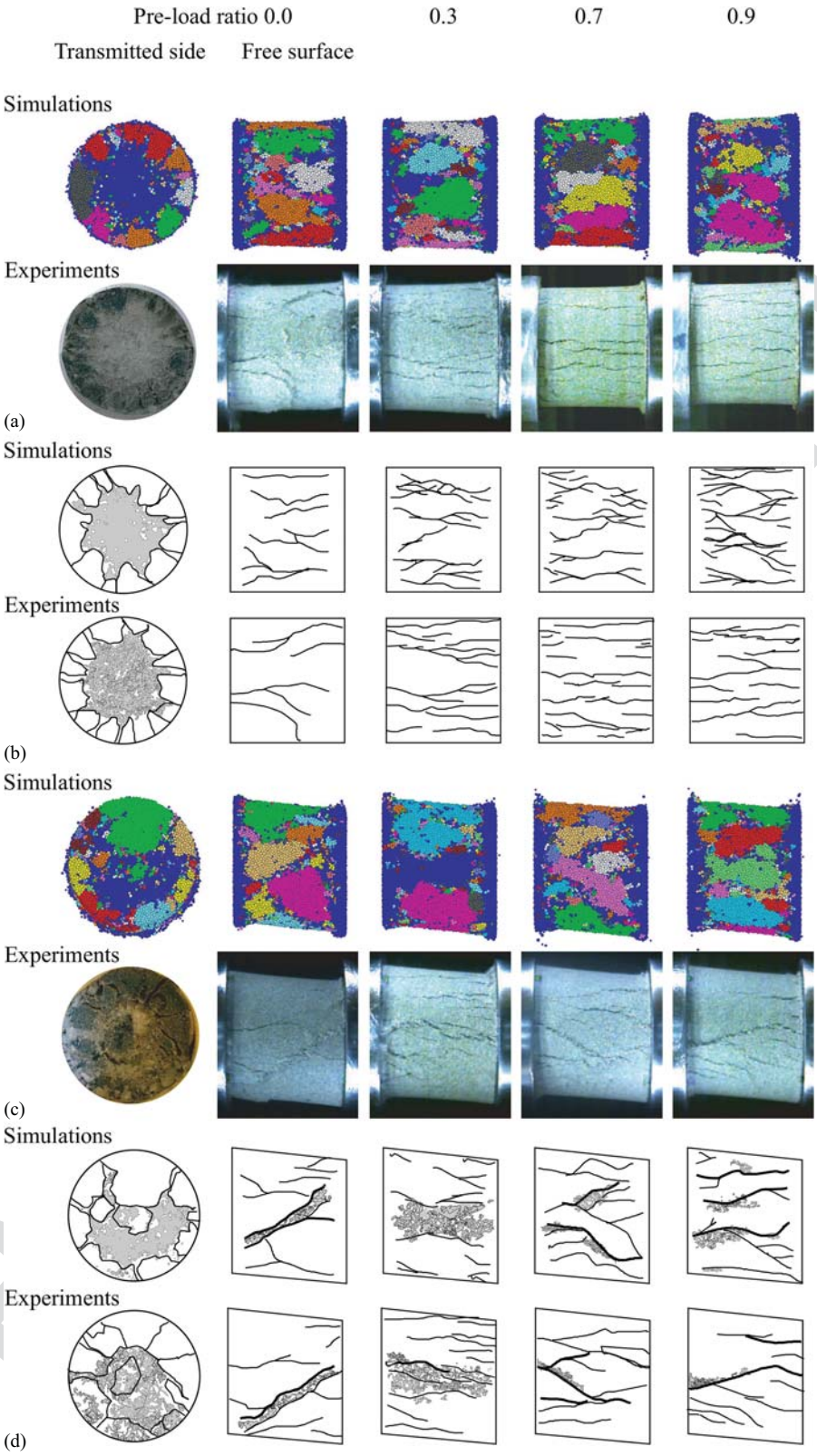

F16:1 F16:2 F16:3 **Fig. 16.** Fragmentation of (a and b) 0°; and (c and d) 7° specimens under combined static-dynamic loading obtained from experiments and simulations. The prevailing fractures (black solid lines) and debris (grey area) are sketched in (b) and (d). The loading rate approximates 3,000 GPa/s; the incident bar is on the right.

677 with the nonadverse effect of the preload on the dynamic equilib-
678 rium discussed in the previous section. Until t_t, a considerable num-
679 ber of microcracks had initiated and coalesced along the
680 preferential failure path. The nucleation of the microcracks induced
681 irreversible damage, which marked the transition from the linear
682 elastic deformation to nonlinear deformation. At t_p, the sample
683 was penetrated by the growing nucleation and hence lost its capac-
684 ity to resist further load. Thereafter, cracks coalesced and nucleated

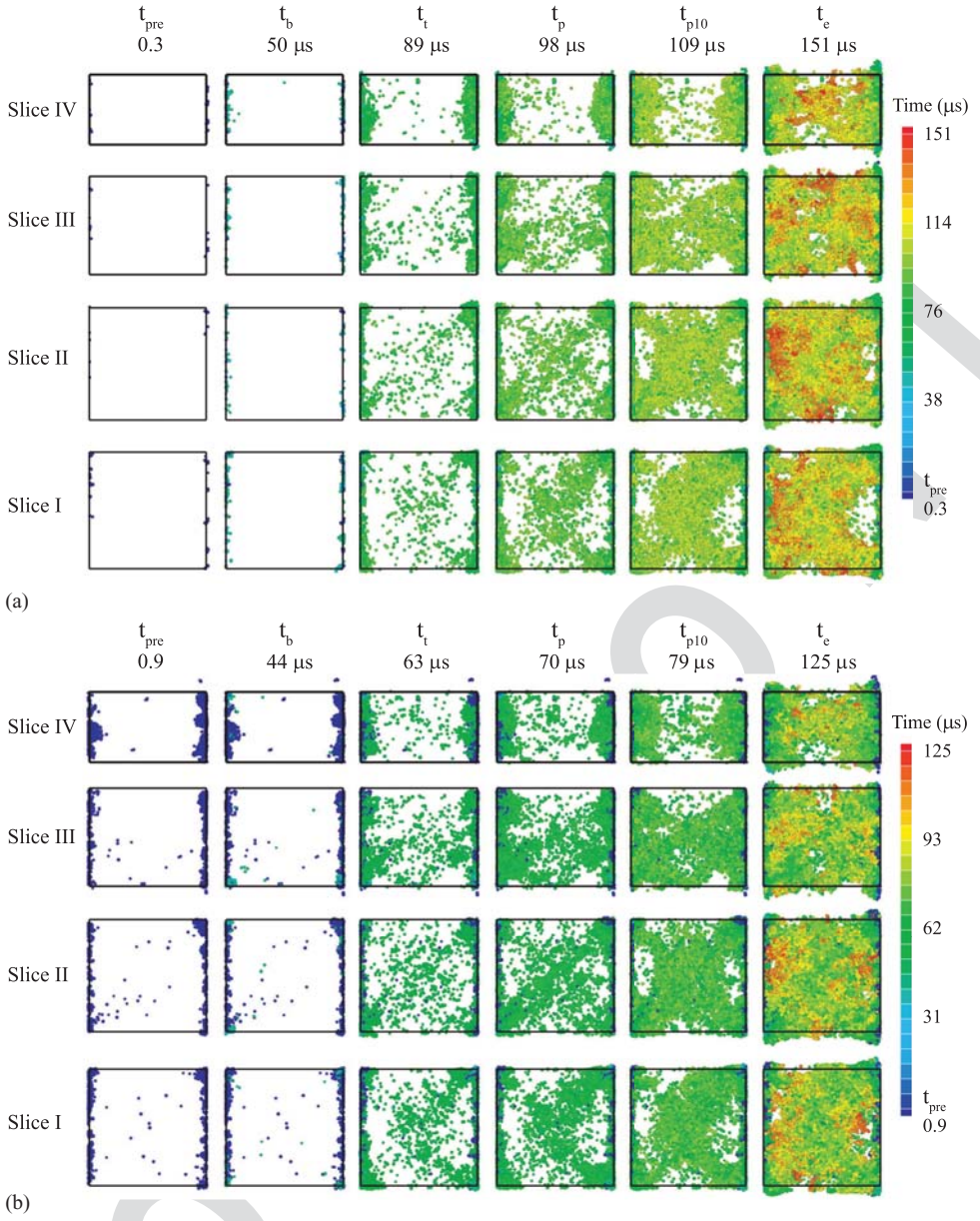

F17:1 F17:2 **Fig. 17.** Spatial and temporal distribution of the simulated microcracks of 0° specimens under combined static-dynamic loading, at the preload ratio and equivalent loading rate of (a) 0.3 and 1,927 GPa/s; and (b) 0.9 and 1,961 GPa/s, respectively. The incident bar is on the right.

extensively, manifested as unstable fracture propagation at the macroscopic level. At t_e, the sample was pervasively damaged. It was noted that the cracks outside the specimen indicate lateral dilation as well as fragments and debris popping out.

The spatiotemporal distribution of the microcracks contributed to understanding the evolving internal damage and to constructing the three-dimensional fracture profiles that were far from simply extending the surface fracture along the depth of the view. Fig. 17 shows that, while the microcracks near the surface of the 0° specimen coalesced approximately in the axial direction, those in the central zone were not homogeneously distributed, but slightly aggregated along the two diagonals. The X-shape fracture bands hence formed an hourglass-like fracture profile that split the specimen into cones at the end. As the combined result of the surface axial fracture, the detached circumference broke into pieces of lenticels, which presented as strip fragments from the free surface and agreed with what were observed from simulations and experiments [Fig. 16(a)].

The formation and growth of the microcracks in the 7° specimen under a low preload showed the similar phenomenon presented by the 0° specimen that the surface axial fractures existed alongside the internal shear fracture band [Fig. 18(a)]. A micromechanism-based hypothesis was previously proposed to understand the observed axial fracture under the low preload (Xu et al. 2020) that the redistribution of the original voids or fissures and their opening-closing status due to the preloading tended to influence the preferential failure path that would be determined by the dynamic compression-shear load. Although the change of the opening–closing status is not shown in Fig. 18(a), the progressive cracking process of the inclined specimens demonstrates that the microstructures reconstructed at a low preload might be able to dominate the failure pattern near the specimen surface (Slices III and IV) but not enough to change the shear fracture band in the central zone (Slices I and II), where the stress level was higher [Fig. 3(c)].

However, the influence of the reconstructed microstructures could be outperformed by extensively accumulated damage under

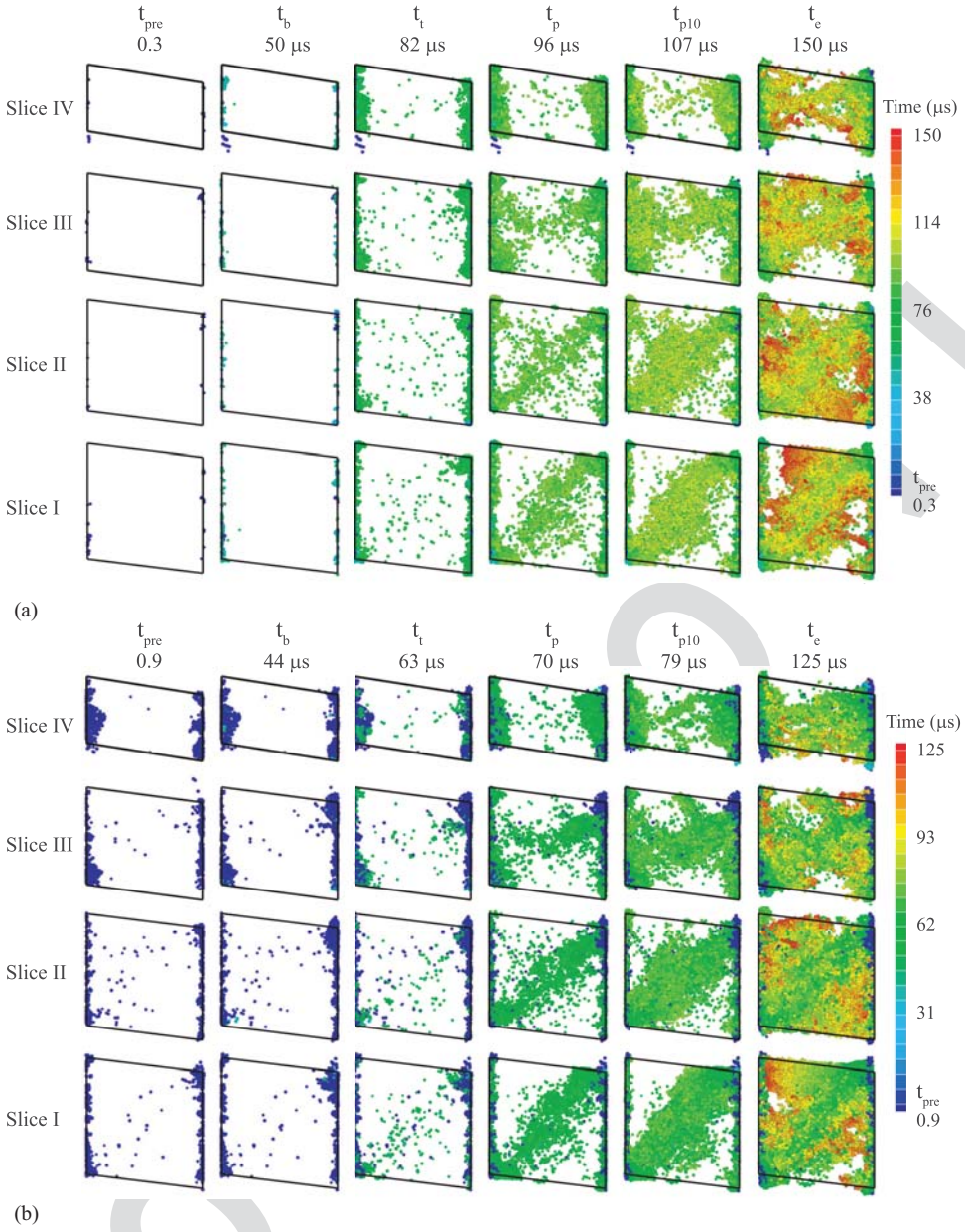

F18:1 F18:2 **Fig. 18.** Spatial and temporal distribution of the simulated microcracks of 7° specimens under combined static-dynamic loading, at the preload ratio and equivalent loading rate of (a) 0.3 and 1,942 GPa/s; and (b) 0.9 and 2,020 GPa/s, respectively. The incident bar is on the right.

a high preload. Fig. 18(b) demonstrates that the formation and coalescence of the dynamic microcracks were guided by the considerable number of microcracks that had initiated on the preferential failure path during preloading. Furthermore, since each slice had the fracture band oriented along its short diagonal, the three-dimensional fracture profile of the inclined specimens resembled a pair of centrosymmetric semicones approximately along the short diagonal, rather than a two-dimensional inclined plane across the central short diagonal. It is worth noting that the inclined specimens failed by the throughgoing fractures that had formed and grown along the short diagonals independently of the damage locally accumulated within the obtuse corners. This was consistent with the simulated results of the 7° specimen under dynamic loading (Xu et al. 2020). Combined with the analysis on stress distribution (see section "Data Reduction Method"), the inclined specimen was verified to comply with the assumption of homogeneous stress distribution within the material failure area.

The effect of the preload on the failure strength and the loading rate, as discussed in the section "Failure Strength and Envelope," was also associated with the micromechanism presented in Figs. 17 and 18. Owing to preloading-induced microstructure redistribution and damage accumulation, the sample material had deteriorated to a certain extent as per the preload ratio before the dynamic loading. As a consequence, the dynamic strength and the loading rate declined at a higher preload. On the other hand, the initial preload contributed to activating the randomly distributed intrinsic flaws such as voids, fissures, pores, and inclusions, resulting in chaos of incipient crack networks that coalesced and nested prior to the dynamic loading. These nonoriented microcracks enabled more materials to participate in resisting the further dynamic loading and required extra energy to generate new surfaces in addition to the major fracture that fatally failed the sample. This was manifested macroscopically with the reinforced total strength and the higher degree of fragmentation under a certain preloading

condition. Since the material deterioration and reinforcement both depended on the preload, there was a turning point of the effect of the preload on the total failure strength.

Conclusions

Experimental and numerical simulations were conducted to understand the compression-shear behaviors of sandstone subjected to combined static-dynamic loads by using inclined specimens in axially constrained SHPB testing. The loading rate of interest ranged from 500 to 4,000 GPa/s, alongside the axial prestress of 7, 21, 35, 49, and 63 MPa on specimens with inclinations of 0°, 3°, 5°, and 7°. Both the experiments and the simulations verified the dynamic equilibrium of inclined specimens in the axially constrained SHPB tests using pulse-shaping techniques, which validated the data processing method. The DEM-based micromechanical modeling reproduced the macroscopical stress–strain relationship and the fragmentation of sandstone specimens under such complex loading conditions.

The failure strength and the Drucker–Prager envelope showed apparent dependence on the loading rate. The failure strength initially increased with the preload and then started experiencing a plateau or slight drop at the preload ratio around 0.7. This turning point was manifested as the upper bound of the failure envelope that expanded with the increasing preload. The double effects of the preload were also shown on the fracturing process at both the bulk scale and the microscale. The spatiotemporal distribution of the microcracks contributed to constructing the interior fracture profiles, which were, however, different from those observed from the specimen surface. The collective influence of the evolving microdamage and the global stress field altered the shear fracturing mode of inclined specimens under dynamic loading, to the axial splitting mode near the specimen surface under low-preload static-dynamic loading, and back to shear fracturing as the preload increased.

Data Availability Statement

All data, models, or code that support the findings of this study are available from the corresponding author upon reasonable request.

Acknowledgments

Funding support from National Natural Science Foundation of China (Nos. 52039007 and 51779164) and Youth Science and Technology Innovation Research Team Fund of Sichuan Province (2020JDTD0001) is gratefully acknowledged.

References

Abou-Sayed, A. S., R. J. Clifton, and L. Hermann. 1976. "The oblique-plate impact experiment." *Exp. Mech.* 16 (4): 110–1120.

Alejano, L. R., and A. Bobet. 2012. "Drucker–Prager criterion." *Rock Mech. Rock Eng.* 45 (6): 995–999. https://doi.org/10.1007/s00603-012-0278-2.

Armstrong, R. W. 1961. "On size effects in polycrystal plasticity." *J. Mech. Phys. Solids* 9 (3): 196–199. https://doi.org/10.1016/0022-5096(61)90018-7.

Armstrong, R. W. 2001. "Plasticity: Grain size effects." In *Encyclopedia of materials: Science and technology*, edited by K. H. J. Buschow, R. W. Cahn, M. C. Flemings, B. Illschner, E. J. Kramer, and S. Mahajan, 7103–7114. Amsterdam, Netherlands: Elsevier.

Branch, M. A., T. F. Coleman, and Y. Li. 1999. "A subspace, interior, and conjugate gradient method for large-scale bound-constrained minimization problems." *SIAM J. Sci. Comput.* 21 (1): 1–23. https://doi.org/10.1137/S1064827595289108.

Cadoni, E., M. Dotta, D. Forni, G. Riganti, and C. Albertini. 2015. "First application of the 3D-MHB on dynamic compressive behavior of UHPC." *EPJ Web Conf.* 94: 01031. https://doi.org/10.1051/epjconf/20159401031.

Chattaraj, R., S. K. Samal, and N. C. Mahanti. 2013. "Dispersion of love wave propagating in irregular anisotropic porous stratum under initial stress." *Int. J. Geomech.* 13 (4): 402–408. https://doi.org/10.1061/(ASCE)GM.1943-5622.0000230.

Chen, R., W. Yao, F. Lu, and K. Xia. 2018. "Evaluation of the stress equilibrium condition in axially constrained triaxial SHPB tests." *Exp. Mech.* 58 (3): 527–531. https://doi.org/10.1007/s11340-017-0344-5.

Chen, W., and G. Ravichandran. 1997. "Dynamic compressive failure of a glass ceramic under lateral confinement." *J. Mech. Phys. Solids* 45 (8): 1303–1328. https://doi.org/10.1016/S0022-5096(97)00006-9.

Christensen, R. J., S. R. Swanson, and W. S. Brown. 1972. "Split-Hopkinson-bar tests on rock under confining pressure." *Exp. Mech.* 12 (11): 508–513. https://doi.org/10.1007/BF02320747.

Dai, F., S. Huang, K. Xia, and Z. Tan. 2010. "Some fundamental issues in dynamic compression and tension tests of rocks using split Hopkinson pressure bar." *Rock Mech. Rock Eng.* 43 (6): 657–666. https://doi.org/10.1007/s00603-010-0091-8.

Dai, F., B. Li, N. Xu, Y. Fan, and C. Zhang. 2016a. "Deformation forecasting and stability analysis of large-scale underground powerhouse caverns from microseismic monitoring." *Int. J. Rock Mech. Min. Sci.* 86: 269–281. https://doi.org/10.1016/j.ijrmms.2016.05.001.

Dai, F., Y. Xu, T. Zhao, N. Xu, and Y. Liu. 2016b. "Loading-rate-dependent progressive fracturing of cracked chevron-notched Brazilian disc specimens in split hopkinson pressure bar tests." *Int. J. Rock Mech. Min. Sci.* 88: 49–60. https://doi.org/10.1016/j.ijrmms.2016.07.003.

Dorogoy, A., and D. Rittel. 2005a. "Numerical validation of the shear compression specimen. Part I: Quasi-static large strain testing." *Exp. Mech.* 45 (2): 167–177. https://doi.org/10.1007/BF02428190.

Dorogoy, A., and D. Rittel. 2005b. "Numerical validation of the shear compression specimen. Part II: Dynamic large strain testing." *Exp. Mech.* 45 (2): 178–185. https://doi.org/10.1007/BF02428191.

Drucker, D. C., and W. Prager. 1952. "Soil mechanics and plastic analysis or limit design." *Q. Appl. Math.* 10 (2): 157–165. https://doi.org/10.1090/qam/48291.

Du, H. B., F. Dai, Y. Xu, Y. Liu, and H. Xu. 2018. "Numerical investigation on the dynamic strength and failure behavior of rocks under hydrostatic confinement in SHPB testing." *Int. J. Rock Mech. Min. Sci.* 108: 43–57. https://doi.org/10.1016/j.ijrmms.2018.05.008.

Du, H. B., F. Dai, Y. Xu, Z. Yan, and M. D. Wei. 2020. "Mechanical responses and failure mechanism of hydrostatically pressurized rocks under combined compression-shear impacting." *Int. J. Mech. Sci.* 165: 105219. https://doi.org/10.1016/j.ijmecsci.2019.105219.

Fairbairn, E. M. R., and F. J. Ulm. 2002. "A tribute to Fernando LLB Carneiro (1913–2001), engineer and scientist who invented the Brazilian test." *Mater. Struct.* 35: 195–196.

Farbaniec, L., J. D. Hogan, K. Y. Xie, M. Shaeffer, K. J. Hemker, and K. T. Ramesh. 2017. "Damage evolution of hot-pressed boron carbide under confined dynamic compression." *Int. J. Impact Eng.* 99: 75–84. https://doi.org/10.1016/j.ijimpeng.2016.09.008.

Field, J. E., S. M. Walley, W. G. Proud, H. T. Goldrein, and C. R. Siviour. 2004. "Review of experimental techniques for high rate deformation and shock studies." *Int. J. Impact Eng.* 30 (7): 725–775. https://doi.org/10.1016/j.ijimpeng.2004.03.005.

Forquin, P., G. Gary, and F. Gatuingt. 2008. "A testing technique for concrete under confinement at high rates of strain." *Int. J. Impact Eng.* 35 (6): 425–446. https://doi.org/10.1016/j.ijimpeng.2007.04.007.

Frew, D. J., S. A. Akers, W. Chen, and M. L. Green. 2010. "Development of a dynamic triaxial Kolsky bar." *Meas. Sci. Technol.* 21 (10): 105704–13. https://doi.org/10.1088/0957-0233/21/10/105704.

Gama, B. A., S. L. Lopatnikov, and J. W. Gillespie. 2004. "Hopkinson bar experimental technique: A critical review." *Appl. Mech. Rev.* 57 (4): 223–250. https://doi.org/10.1115/1.1704626.

Gong, F. Q., X. F. Si, X. B. Li, and S. Y. Wang. 2019. "Dynamic triaxial compression tests on sandstone at high strain rates and low confining pressures with split Hopkinson pressure bar." *Int. J. Rock Mech. Min. Sci.* 113: 211–219. https://doi.org/10.1016/j.ijrmms.2018.12.005.

Gupta, Y. M. 1983. "Shear and compression wave measurements in shocked polycrystalline Al_2O_3." *J. Geophys. Res.: Solid Earth* 88 (B5): 4304–4312. https://doi.org/10.1029/JB088iB05p04304.

Hazzard, J. F., and R. P. Young. 2000. "Simulating acoustic emissions in bonded-particle models of rock." *Int. J. Rock Mech. Min. Sci.* 37 (5): 867–872. https://doi.org/10.1016/S1365-1609(00)00017-4.

Hazzard, J. F., R. P. Young, and S. C. Maxwell. 2000. "Micromechanical modeling of cracking and failure in brittle rocks." *J. Geophys. Res.: Solid Earth* 105 (B7): 16683–16697. https://doi.org/10.1029/2000JB900085.

Hoek, E., and E. T. Brown. 1980. *Underground excavations in rock*, 93–101. Boca Raton, FL: CRC Press.

Hokka, M., J. Black, D. Tkalich, M. Fourmeau, A. Kane, N. H. Hoang, C. C. Li, W. W. Chen, and V. T. Kuokkala. 2016. "Effects of strain rate and confining pressure on the compressive behavior of Kuru granite." *Int. J. Impact Eng.* 91: 183–193. https://doi.org/10.1016/j.ijimpeng.2016.01.010.

Jiang, R. C., F. Dai, Y. Liu, and A. Li. 2021. "Fast marching method for microseismic source location in cavern-containing rockmass: Performance analysis and engineering application." *Engineering*. https://doi.org/10.1016/j.eng.2020.10.019.

Jing, L. 2003. "A review of techniques, advances and outstanding issues in numerical modelling for rock mechanics and rock engineering." *Int. J. Rock Mech. Min. Sci.* 40 (3): 283–353. https://doi.org/10.1016/S1365-1609(03)00013-3.

Khazaei, C., J. Hazzard, and R. Chalaturnyk. 2015. "Damage quantification of intact rocks using acoustic emission energies recorded during uniaxial compression test and discrete element modeling." *Comput. Geotech.* 67: 94–102. https://doi.org/10.1016/j.compgeo.2015.02.012.

Khosravi, A., and R. Simon. 2018. "Verification of the CSDS model in estimating the postpeak behavior of hard rocks." *Int. J. Geomech.* 18 (3): 04017166. https://doi.org/10.1061/(ASCE)GM.1943-5622.0001090.

Li, A., N. Xu, F. Dai, G. Gu, Z. Hu, and Y. Liu. 2018a. "Stability analysis and failure mechanism of the steeply inclined bedded rock masses surrounding a large underground opening." *Tunnelling Underground Space Technol.* 77: 45–58. https://doi.org/10.1016/j.tust.2018.03.023.

Li, B., N. Xu, F. Dai, G. Zhang, and P. Xiao. 2019. "Dynamic analysis of rock mass deformation in large underground caverns considering microseismic data." *Int. J. Rock Mech. Min. Sci.* 122: 104078. https://doi.org/10.1016/j.ijrmms.2019.104078.

Li, X. B., Z. L. Zhou, T. S. Lok, L. Hong, and T. B. Yin. 2008. "Innovative testing technique of rock subjected to coupled static and dynamic loads." *Int. J. Rock Mech. Min. Sci.* 45 (5): 739–748. https://doi.org/10.1016/j.ijrmms.2007.08.013.

Li, X. F., Q. B. Zhang, H. B. Li, and J. Zhao. 2018b. "Grain-based discrete element method (gb-dem) modelling of multi-scale fracturing in rocks under dynamic loading." *Rock Mech. Rock Eng.* 51 (12): 3785–3817. https://doi.org/10.1007/s00603-018-1566-2.

Lindholm, U. S., L. M. Yeakley, and A. Nagy. 1974. "The dynamic strength and fracture properties of dresser basalt." *Int. J. Rock Mech. Min. Sci. Geomech. Abstr.* 11 (5): 181–191. https://doi.org/10.1016/0148-9062(74)90885-7.

Liu, K., J. Zhao, G. Wu, A. Maksimenko, A. Haque, and Q. B. Zhang. 2020. "Dynamic strength and failure modes of sandstone under biaxial compression." *Int. J. Rock Mech. Min. Sci.* 128: 104260. https://doi.org/10.1016/j.ijrmms.2020.104260.

Nguyen, N. H. T., H. H. Bui, G. D. Nguyen, and J. Kodikara. 2017. "A cohesive damage-plasticity model for DEM and its application for numerical investigation of soft rock fracture properties." *Int. J. Plast.* 98: 175–196. https://doi.org/10.1016/j.ijplas.2017.07.008.

Nie, X., W. W. Chen, X. Sun, and D. W. Templeton. 2007. "Dynamic failure of borosilicate glass under compression/shear loading experiments." *J. Am. Ceram. Soc.* 90 (8): 2556–2562. https://doi.org/10.1111/j.1551-2916.2007.01819.x.

Paliwal, B., and K. T. Ramesh. 2008. "An interacting micro-crack damage model for failure of brittle materials under compression." *J. Mech. Phys. Solids* 56 (3): 896–923. https://doi.org/10.1016/j.jmps.2007.06.012.

Paliwal, B., K. T. Ramesh, J. W. McCauley, and M. Chen. 2008. "Dynamic compressive failure of alon under controlled planar confinement." *J. Am. Ceram. Soc.* 91 (11): 3619–3629. https://doi.org/10.1111/j.1551-2916.2008.02712.x.

Pierron, F., and M. Grédiac. 2012. *The virtual fields method: Extracting constitutive mechanical parameters from full-field deformation measurements*, 3–19. New York: Springer.

Potyondy, D. O., and P. A. Cundall. 2004. "A bonded-particle model for rock." *Int. J. Rock Mech. Min. Sci.* 41 (8): 1329–1364. https://doi.org/10.1016/j.ijrmms.2004.09.011.

Ranjith, P. G., J. Zhao, M. Ju, R. V. S. De Silva, T. D. Rathnaweera, and A. K. M. S. Bandara. 2017. "Opportunities and challenges in deep mining: A brief review." *Engineering* 3 (4): 546–551. https://doi.org/10.1016/J.ENG.2017.04.024.

Scholtès, L., and F. V. Donzé. 2013. "A DEM model for soft and hard rocks: Role of grain interlocking on strength." *J. Mech. Phys. Solids* 61 (2): 352–369. https://doi.org/10.1016/j.jmps.2012.10.005.

Weatherley, D., V. Boros, and W. Hancock. 2011. *ESyS-particle tutorial and user's guide version 2.1*. Brisbane, Australia: Earth Systems Science Computational Centre, Univ. of Queensland.

Weng, L., X. Li, X. Shang, and X. Xie. 2018. "Fracturing behavior and failure in hollowed granite rock with static compression and coupled static-dynamic loads." *Int. J. Geomech.* 18 (6): 04018045. https://doi.org/10.1061/(ASCE)GM.1943-5622.0001132.

Xu, Y., and F. Dai. 2018. "Dynamic response and failure mechanism of brittle rocks under combined compression-shear loading experiments." *Rock Mech. Rock Eng.* 51 (3): 747–764. https://doi.org/10.1007/s00603-017-1364-2.

Xu, Y., F. Dai, and H. Du. 2020. "Experimental and numerical studies on compression-shear behaviors of brittle rocks subjected to combined static-dynamic loading." *Int. J. Mech. Sci.* 175: 105520. https://doi.org/10.1016/j.ijmecsci.2020.105520.

Zhang, P., Z. Meng, K. Zhang, and S. Jiang. 2020. "Impact of coal ranks and confining pressures on coal strength, permeability, and acoustic emission." *Int. J. Geomech.* 20 (8): 04020135. https://doi.org/10.1061/(ASCE)GM.1943-5622.0001752.

Zhang, Q. B., and J. Zhao. 2014. "A review of dynamic experimental techniques and mechanical behaviour of rock materials." *Rock Mech. Rock Eng.* 47 (4): 1411–1478. https://doi.org/10.1007/s00603-013-0463-y.

Zhao, T., F. Dai, N. W. Xu, Y. Liu, and Y. Xu. 2015. "A composite particle model for non-spherical particles in DEM simulations." *Granular Matter* 17 (6): 763–774. https://doi.org/10.1007/s10035-015-0596-7.

Zhou, L., S. Xu, J. Shan, Y. Liu, and P. Wang. 2018. "Heterogeneity in deformation of granite under dynamic combined compression/shear loading." *Mech. Mater.* 123: 1–18. https://doi.org/10.1016/j.mechmat.2018.04.013.

Zhou, Y. X., K. Xia, X. B. Li, H. B. Li, G. W. Ma, J. Zhao, Z. L. Zhou, and F. Dai. 2012. "Suggested methods for determining the dynamic strength parameters and mode-I fracture toughness of rock materials." *Int. J. Rock Mech. Min. Sci.* 49: 105–112. https://doi.org/10.1016/j.ijrmms.2011.10.004.

Queries

1. Please provide the ASCE Membership Grades for all authors who are members.

2. Please confirm whether it is correct for the term ‘static dynamic’ to be hyphenated, or whether ‘static’ and ‘dynamic’ are in fact two different terms of equal weight and therefore the term should be joined by an en rule throughout.

3. There are two references (Li et al. 2018a, b) in the reference list with identical author surnames and years; hence, to avoid ambiguity, we have added designators “a” and “b” along with the year in the list. As their citations in the text do not reflect this change, in the sentence beginning “DEM has been successfully developed…,” please specify whether “Li et al. (2018)” refers to “Li et al. (2018a)” or “Li et al. (2018b).”

4. There are two references (Li et al. 2018a, b) in the reference list with identical author surnames and years; hence, to avoid ambiguity, we have added designators “a” and “b” along with the year in the list. As their citations in the text do not reflect this change, in the sentence beginning “Such a stress range covered the extreme…,” please specify whether “Li et al. (2018)” refers to “Li et al. (2018a)” or “Li et al. (2018b).”

5. Please confirm whether our amendment of this term throughout is correct for your intended meaning.

6. In sentence starting ‘The loading rate’, the meaning is unclear in the text ‘while the failure strength the peak value’. Is there a word missing after ‘strength’? Please clarify.

7. We have amended the text here slightly for sense; please confirm whether our changes are correct for your intended meaning.

8. In the sentence starting ‘The dynamic force on the incident side’, meaning unclear in the text ‘while the force on the transmitted side directly the transmitted wave’. Is there a word missing after ‘directly’?

9. Please clarify the meaning here.

10. Readers of print will only see figures in black and white. Please modify your text accordingly in the sentence beginning “In simulations, particles that constituted2.

11. Readers of print will only see figures in black and white. Please modify your text accordingly in the sentence beginning “In particular, particles in blue”.

12. Please provide volume number and page range for reference “Jiang et al. (2021)” references list entry.

13. References “Li et al. (2018a, b)” is listed in the reference list but not cited in the text. Please cite in the text, else delete from the list.

14. Please add a column header to the first column in Table 1.

15. Please note that the format of Tables 6 and 7 has been modified.

16. Please provide the part label descriptions in caption for Fig. 10.